Reactive DC Magnetron Sputtering of Ultrathin Superconducting Niobium Nitride Films

by Andrew E. Dane

S.B. Engineering Sciences

Harvard University, 2010

Submitted to the department of Electrical Engineering and Computer Science in partial fulfillment of the requirements for the degree of:

Master of Science in Electrical Engineering

At the

Massachusetts Institute of Technology

February 2015

©2015 Massachusetts Institute of Technology

The author hereby grants to MIT permission to reproduce and to distribute publicly paper and electronic copies of this thesis document in whole or in part in any medium now known or hereafter created

Signature of Author:..

Department of Electrical Engineering and Computer Science

January 31st 2015

Certified by:..

Karl K. Berggren

Professor of Electrical Engineering

Thesis Supervisor

Accepted by:..

Leslie Kolodziejski

Professor of Electrical Engineering and Computer Science

Chairman of the Committee on Graduate Students

Reactive DC Magnetron Sputtering of

Ultrathin Superconducting Niobium Nitride Films

by Andrew E. Dane

Abstract:

DC reactive magnetron sputtering was used to deposit few-nanometer-thick films of niobium nitride for fabrication of superconducting devices. Over 1000 samples were deposited on a variety of substrates, under various chamber conditions. Sheet resistance, thickness and superconducting critical temperature were measured for a large number of samples. Film Tc was improved by changing the way the samples were heated during the deposition, by ex situ rapid thermal processing, and in some cases by the addition of an RF bias to the substrate holder during the sputter deposition. These improvements to the deposition of NbN have enabled the production of superconducting nanowire single photon detectors whose quantum efficiency saturates and was the starting point for work on the superconductor-insulator transition.

Thesis Advisor: Karl K. Berggren

Title: Professor of Electrical Engineering

Acknowledgements:

I would like to thank the following people for their help in making this thesis possible:

Professor Karl Berggren, for all of his help and support.

Jim Daley and Mark Mondol who work tirelessly to keep the NSL running smoothly.

The students of the QNN group, especially the SNSPD team: Francesco Bellei, Adam McCaughan, Faraz Najafi, Kristen Sunter and Qingyuan Zhao.

The Dane, Lu and Lonsdale families.

Thank you!

Table of Contents:

1. Introduction 1
2. Superconducting and material properties of NbN 3
    a. History and Uses of NbN 3
    b. Normal-Metal Properties of NbN 4
    c. Superconducting Material Properties Review 5
    d. Critical Temperature of NbN 9
    e. Penetration Depth of NbN 11
    f. Coherence Length of NbN 12
    g. Methods of Producing NbN films 13
    h. Optical Properties of Sputtered NbN 13
    i. References 14
3. Sputtering Basics 22
    a. Plasma Basics 22
    b. DC Sputtering 28
    c. Magnetron Sputtering 30
    d. Other Sputtering Conditions 33
    e. RF Sputtering 34
    f. Reactive Sputtering 38
    g. Structure-Zone Models 41
    h. Stress in Sputtered Films 43
    i. Bias Sputtering 45
    j. Conclusions 46
    k. References 47
4. Methods 51
    a. Substrate Preparation 51
    b. DC Reactive Magnetron Sputtering 53
    c. Sheet Resistance 56
    d. Measuring the Superconducting Critical Temperature 57
    e. Transmissometry 59
    f. X-ray Reflectivity 59

g. Rapid Thermal Processing 60

5. Experimental Results and Discussion 61

a. Reproducibility: Short-Term, Among Substrates, and Long-Term 62

b. Tc of NbN on SiNx and SiO_2 63

c. Long-Term Reproducibility 65

d. Design of Experiments 69

e. Improving the Substrate Holder 74

f. Backside Absorber 75

g. Bias Sputtering 78

h. Rapid Thermal Processing 80

i. X-ray Reflectivity 86

j. Rapid Thermal Processing of Room Temperature Deposited Nb and NbN 88

k. References 95

6. Conclusions 98

a. References 100

Chapter 1

Introduction:

Niobium nitride (NbN) has a bulk superconducting transition temperature (T_c) close to 16 K, however the T_c of thin films of niobium nitride suitable for applications is often suppressed, and for few-nanometer thick films, the thinner the film, the lower the T_c. This means that superconducting devices that benefit from being made thinner must do so at the expense of T_c, and at a fixed operating temperature this means lower critical currents, lower critical fields and more dissipation for dynamical signals. Additionally, reproducibility of the properties of sputtered NbN has been limited, hampering device engineering. In this thesis we attempted to maximize the T_c of ultrathin film NbN deposited by DC reactive magnetron sputtering onto silicon based substrates by varying the sputtering conditions and using ex-situ rapid thermal processing. We also characterized the reproducibility of the T_c of the films produced.

Before discussing the results of this work we first review some basic superconductivity concepts as well as properties of superconducting Niobium Nitride in chapter two. Important superconducting length scales are emphasized and some basics of the microscopic BCS theory and phenomenological Ginsburg landau theory are presented. Experimental work on NbN is highlighted to give interested parties a full picture of what is known; a great deal of literature has been published, and continues to be published, on NbN since its discovery as a superconductor in 1941.

Chapter three goes into detail about basic plasma physics, DC, RF, and magnetron sputtering. Reactive sputtering is discussed as it is essential for creating high quality NbN. Reactive sputtering of NbN from a high purity Niobium target minimizes impurities in the resulting film and allows for control

over stoichiometry by varying the reactive gas flow and pressure. Plasma environments without reactive gases are complex; the addition of a reactive gas can make the chamber conditions and the effect on the deposited film difficult to predict or control without knowledge of the basic processes.

Results are summarized in chapter five, and are based on the methods described in chapter four. Over 1000 few-nanometer-thick NbN films were deposited by DC reactive magnetron sputtering on a variety of substrates under a variety of conditions. Transport measurements were made at room and low temperature, with the film superconducting temperature being one of the focuses of our efforts to develop a reliable material system. The main results of this work include: (1) establishing the conditions for reproducibility in the properties of our films, an issue that plagued us in the past but seems significantly improved when using amorphous substrates, (2) improvement of film T_c by direct heating of substrates with the halogen lamp heaters inside of the deposition chamber, (3) improvement of film T_c through the use of rapid thermal processing.

This work on NbN deposition has enabled the fabrication of NbN superconducting nanowire single photon detectors which exhibit saturating internal quantum efficiency, as well as other superconducting nano-devices. These will not be discussed in what follows.

Chapter 2

Superconducting and Material Properties of Niobium Nitride:

The interpretation of the results of this thesis and their use in designing and fabricating useful devices rely on knowing some basics of superconductivity. Many of the useful properties of superconductors are not experimentally accessible as process control variables that would make sense for engineering purposes. For instance, the superconducting gap of a thin film can be measured directly, either by measuring the differential conductance of a tunnel junction fabricated from the material or by taking scanning tunneling microscopy measurements of the film. Knowledge of the gap can then be employed to estimate the size of the quasiparticle cloud created after a photon is absorbed by a superconductor, which can enable the design of efficient superconducting nanowire single photon detectors, for instance. However, both of the aforementioned avenues for measuring the gap are costly and effort intensive, especially when reproducibility is an issue and large numbers of samples need to be measured. Instead of measuring the gap of the superconductor directly, it will suffice to measure the T_c of the material and relate the Tc to the superconducting gap through well-known relations from BCS theory.

Similar statements can be made about device kinetic inductance which can be estimated using the T_c and resistivity, as will be mentioned below.

History and Uses of NbN:

Niobium nitride was first discovered to be a superconductor in 1941 [1]. World War II made it difficult for early discoveries involving NbN to be communicated widely [2]. It had the highest known T_c until 1953, when it was supplanted by V_3Si [3], which has a T_c of about 17K, which was itself surpassed by Nb_3Sn, which has a maximum T_c of 18.3K, a year later [4]. Original reports of NbN's T_c were conflicting and contradictory until, in 1952, Rogener [5] showed that the T_c of NbN_x is highly dependent on the relative amounts of Niobium and Nitrogen in the compound. Since Rogener's discovery, it has been recognized that the electrical and superconducting properties of NbN are dependent on a number of factors including: composition, crystal phase, and crystallinity.

NbN has been used to make a variety of superconducting devices including hot electron bolometers [6], superconducting nanowire single photon detectors [7], Josephson junctions [8], SQUIDs [9], a variety of RSFQ circuits [10], as well as three terminal superconducting transistor-like devices [11]. NbN has also been used in a variety of resonators [12], RF cavities [13], delay lines and other electrical circuits [14] which benefit from the low loss of a superconducting component as well as the kinetic inductance of thin film superconductors.

Normal-Metal Properties of NbN:

The bulk normal properties of NbN can be summarized as follows. NbN is a metallic gray compound with a bulk resistivity in the neighborhood of 60 to 80 μOhm*centimeters [15]. The mean free path of an electron in NbN is about 4 Angstroms, estimated using measured resistivity and a free electron model. The crystalline phases of NbN have been difficult to establish experimentally due to the large number of crystal phases. Numerous different phases exist at different temperatures and nitrogen to niobium ratios and within a phase the ratio of non-metal to metal is associated with different crystal lattice constants [16]. The delta phase of NbN, also referred to as B1 or NaCl-type crystal lattice, has the highest T_c among NbN polymorphs and among B1 type superconductors [17]. The band structure of NbN has been calculated using linear combination of atomic orbitals (LCAO) and augmented plane wave methods [18] to determine a density of states at the Fermi energy (N(0)) to be 0.54 states/(eV*m^3); experimentally determined values have been shown that corroborate this number, however others have values almost half as much. The difference is attributed to the samples being non-stoichiometric.

Superconducting Material Properties Review:

The superconducting critical temperature is the temperature at which an ideal superconducting material loses all resistance and it is one of, if not the key, superconducting material property. In the presence of thermal fluctuations, the transition from normal metal to superconducting as the temperature is reduced is not immediate. Instead, the transition will have a measurable width. In measurements of resistance versus temperature, the critical temperature is usually defined by convention as the temperature at which the resistance has fallen to some fraction of its normal state resistance. The critical temperature is one of the most important

properties of a superconductor, especially for applications, since the necessary cooling system can vary significantly in cost depending on the temperature needed. Bardeen-Cooper-Schrieffer (BCS) theory explained superconductivity by showing how electrons in a crystal lattice could form pairs of non-scattering charge carriers via electron phonon interaction. At high temperature, thermal energy and increased scattering prevents pairing, but at low enough temperature the formation of these Cooper pairs gives rise to superconductivity. The predictions of BCS theory have explained a wide variety of the behavior of low temperature superconductors including the isotope effect which confirms the role of phonons in pairing. BCS theory gives us the following relationship for T_c:

$$k_B T_c = 1.13\hbar\omega_D e^{-1/N(0)V}$$

Here ω_D is the Debye frequency, $N(0)$ is the density of states at the Fermi level and V is the electron-phonon coupling constant, all for the material being considered. This formula is valid in the weak coupling limit where $N(0)V << 1$.

The superconducting energy gap is the gap that appears at the Fermi energy in the density of states of a material that is superconducting. It describes the energy of the bond between electrons in Cooper pairs and can be used to determine the condensation energy of the superconductor, that is, the thermodynamic free energy difference between the sample in the superconducting state and the normal state. The sample will superconduct when the superconducting state minimizes the free energy of the system. For typical low temperature superconductors without magnetic impurities, the gap is zero at T_c and maximal at zero temperature. Once again, BCS theory gives us an expression for the gap in terms of electronic and phononic properties, and in the weak coupling limit, the gap expression is the same as the above expression for $k_B T_c$ to within a numerical constant of order unity. At zero temperature, we

have $\frac{\Delta(0)}{k_B T_c} = 1.764$, where $\Delta(0)$ is the gap at zero temperature. Interestingly, it is in fact possible to have superconductivity even when the gap is equal to zero. The addition of magnetic impurities or other “time-reversal noninvariant perturbations” [19] can suppress the gap to zero while the material continues to superconduct and have zero resistance.

While the critical temperature is an extremely important material property, two additional properties that account for a great deal of a material’s superconducting behavior are the coherence length (ξ) and the penetration depth (λ). Both of these lengths appear in the BCS theory as well as the phenomenological Ginzburg Landau theory, and, confusingly, are mentioned without reference to which theory is being used. In BCS theory, the coherence length describes the length scale over which electrodynamic effects are correlated; the relationship between an electric field and the resulting current density is nonlocal. The BCS coherence length is given by the following expression:

$$\xi_o = \frac{\hbar v_F}{\pi\Delta(0)} = \frac{\hbar v_F}{1.764\pi k_B T_c}$$

Where v_F is the velocity of electrons at the Fermi level. The BCS coherence length can be related to the GL coherence length assuming a free electron model. This yields the following formula for the GL coherence length:

$$\xi_{GL}(T) = \frac{0.74\xi_o}{\sqrt{1 - \frac{T}{T_c}}}$$

The penetration depth is a measure of how far into a bulk superconducting material applied magnetic fields are able to penetrate. Once again, BCS theory allows us to calculate the

value of this parameter. In the local approximation, the case appropriate for NbN, the penetration depth is the same as the London penetration depth to within a numerical constant, c:

$$\lambda = c\sqrt{\frac{m}{\mu_o n e^2}}$$

For NbN, c is approximately 3. This value of the penetration depth can be used to give a temperature dependent expression for use in the Ginzburg Landau theory:

$$\lambda_{GL}(T) = \frac{\lambda}{2\sqrt{1-\frac{T}{T_c}}}$$

The above description of penetration depth and coherence length is correct in the clean limit, which assumes that the mean free path of electrons in the metal is much longer than the coherence length. For many practical superconductors, the mean free path is much less than the coherence length. In this case, known as the dirty limit, the two lengths can be approximated with the following prescription: $\xi_o \rightarrow \sqrt{\xi_o l}$ and $\lambda \rightarrow \lambda\sqrt{\frac{\xi_o}{l}}$ where l is the mean free path. The coherence length becomes the geometric mean between the BCS coherence length and the mean free path, while the penetration depth is scaled by $\sqrt{\frac{\xi_o}{l}}$.

Depending on the relative lengths of the penetration depth and coherence length, the behavior of a given material in a sufficiently strong magnetic field can vary greatly. Type 1 superconductors are those that expel magnetic field completely, until some critical field is reached, at which point superconductivity breaks down. Type 2 superconductors behave like type 1 at low magnetic fields, but above a material dependent field, admit quantized amounts of magnetic flux to penetrate into their bulk. These lines of magnetic flux are surrounded by

circulating current and are referred to as vortices. As the field is turned up, more of these vortices enter the material until at some point superconductivity again breaks down. It can be rigorously shown that for superconductors where $\xi > \sqrt{2}\lambda$, it is energetically favorable for the material to enter the normal state rather than support a vortex, while in the complementary case, superconductivity with vortices is energetically favorable. The former class of materials is type 1, while the latter is type 2.

Since we are mostly interested in thin films of superconducting material, it is worth noting here that the penetration depth for magnetic field perpendicular to the film plane in films whose thickness is much less than the bulk penetration depth is modified. Due to the confinement that the thin film provides, the penetration depth is effectively lengthened to what is known as the Pearl length: $\lambda_P = \frac{\lambda^2}{d}$ where d is the film thickness [20]. Additionally, this change in the effective length of the penetration depth may contribute to type 2 like states in thin films of type 1 materials [21]. This regime, in which there may be radical changes in superconducting behavior due to size effects, was recently described as a “largely unexplored field of mesoscopic type-I superconductors.” [22].

Critical Temperature of NbN:

The relatively high superconducting critical temperature of Niobium Nitride has led to considerable interest and research into its superconducting properties. The bulk superconducting properties of NbN are summarized below. The bulk T_c – though highly dependent on chemical composition, crystal phase, and defect density – is generally considered to be about 16K [23].

The effect that the ratio of nitrogen to niobium in a sample of NbN_x has on the T_c was first explored in 1952 [5]. In most studies, it is claimed that a one-to-one ratio of niobium to nitrogen yields the highest T_c, however other results indicate that deviations from stoichiometry increase T_c; in particular, ref 24 showed that a composition of $NbN_{0.93}$ had a T_c about 400 mK higher than $NbN_{0.99}$. Nb(CN) has been shown to have a higher T_c than NbN; the addition of contaminates such as carbon can enhance the T_c of NbN compounds, further complicating this determination [25].

The effect of vacancies on the T_c of NbN was probed by irradiating various niobium compounds, including NbN, NbCN, and NbC with a varying dose of 1MeV neutrons. [26]. At the highest dose tested, $1.5 \times 10^{20}/\text{cm}^2$, the midpoint T_c of the NbN sample was reduced by only 8%, from 15.5K, compared to up to 26% for the other compounds and up to 80% for the high T_c A15 crystal phase superconductors, like Nb_3Sn. In a different study, it was shown that neutron bombardment could lead to an order of magnitude increase in NbN critical current in the presence of a range of magnetic fields, likely due to the creation of pinning centers [27]. The reduction in T_c agrees with a proposed model relating vacancies in the Niobium and Nitrogen sublattices to the T_c , via the number of valence electrons per atom [28]. These results are similar to those for other low-temperature superconductors with the B1 crystal structure, such as TiO. The superconducting critical temperature is a strong function of the number of vacancies in the crystal lattice [29]. Stoichiometric samples were treated with high temperatures (up to 1650 °C) and high pressures, up to 90 kbar, to remove vacancies from the crystal lattice. While initial samples had 15% vacancies in all lattice sites and T_c close to 0.8K, samples with 0% vacancies had T_c of 2.3K. Interestingly, the lower the concentration of vacancies, the greater the lattice parameter of the TiO sample, indicating that the vacancies require less space in the crystal than a

titanium or oxygen molecule. This also shows that in the TiO system there is a strong correlation between lattice parameter and T_c, similar to what has been observed in NbN.

The T_c of bulk or thick film niobium nitride is well predicted by the strong coupling McMillan formula, which takes into account higher order interactions beyond the simple BCS expression:

$$k_B T_c = \frac{\hbar\omega_D}{1.45} e^{-\left(\frac{1.04(1+N(0)V)}{N(0)(V-U_c[1+0.62N(0)V])}\right)}$$

where ω_D is the Debye frequency, $N(0)$ is the band structure density of electron states, V is the electron phonon interaction parameter, and U_c is the screened coulomb interaction parameter [30]. The McMillan formula predicts that increasing ω_D, V and $N(0)$ will increase T_c. NbN's large T_c in this framework is a result of its large V and ω_D [17].

It was theoretically predicted, using a modified McMillan formula, that the T_c of niobium nitride would increase under pressure [31]. The predicted increase in T_c is due to an increase in the Debye frequency as well as an increase in the electron-phonon coupling. Intrinsic stress in sputtered NbN films has been measured [32], and while compressive stress seems generally associated with higher T_c films, it does not appear to be the leading contribution. This conclusion in thin films is further bolstered by explicit measurements of the critical current of a NbN sample versus strain, where no variation of the critical current was found up to 0.7% strain in a variety of magnetic fields [33]. NbN's tolerance to stress and strain is unfortunate because stress can be widely varied by changing the deposition pressure while sputtering [34] or adding ion bombardment [35].

The effects of film thickness on T_c of NbN is nicely summarized in [36] and [37]. The dominant mechanism by which the T_c is suppressed is still being explored. The effect of disorder on the T_c of NbN films appears is connected to the thickness and sheet resistance related suppression of T_c and the superconductor insulator transition.

Penetration Depth of NbN:

Measurements of the penetration depth in 540 nm thick films of NbN yielded a zero temperature penetration depth of 194 nm [38]. This value for the penetration depth is in contrast to earlier measurements, which concluded that the zero temperature penetration depth was almost twice as long, 385 nm [39]. While the film from the earlier measurement was 800nm thick, its T_c was 15.3K, whereas the film used by Komiyama et al had a T_c of 16K. The difference in penetration depth is likely resolved by the differences in the film resistivity and T_c, since the effective penetration depth can be expressed as a function of both [40]: $\lambda_{eff} = 1.05 \times 10^{-5} \sqrt{\frac{\rho_n}{T_c}}$ (cm), where ρ_n is the normal state resistivity in micro-ohm centimeters.

The penetration depth in relatively thick films of NbN has been estimated from the T_c, resistivity, and the strong coupling parameter [41] to yield a value of 176nm at zero temperature. A particularly helpful relation for the GL penetration depth in the dirty limit as a function of temperature is given in ref [42]: $\lambda_{GL} = 6.42 \times 10^{-6} \sqrt{\frac{\rho_n}{T_c}} \frac{1}{\sqrt{1-\frac{T}{T_c}}}$ where λ_{GL} is in centimeters, and the resistivity is in micro-ohm centimeters. It is unclear where the numerical error between this and the former relation for the penetration length originates. Penetration depths have also been estimated for superconducting films with a variety of lumped resonator methods [43].

Surprisingly, while this study of the penetration depth versus thickness of Nb film incorporates effects due to the resistivity, no mention is made of the effective lengthening of the penetration depth when the film thickness is less than the bulk penetration depth, a situation elucidated by Pearl [20].

Coherence Length of NbN:

The GL coherence length of thin film NbN can be inferred from measurements of H_c2 at zero temperature, as was done in ref [44]. The relevant relation is:

$$\xi_{GL} = \sqrt{\frac{\Phi_o}{2\pi H_{c2}(0)}}$$

Where Φ_o is the magnetic flux quantum, and $H_{c2}(0)$ is the upper critical field at zero temperature. The GL coherence length found with this method varied between 4nm and 8nm as the T_c of the measured film varied between 16K and 3K. In the same work, the BCS coherence length was calculated using the BCS relation for the coherence length in the dirty limit, but it was found to be about twice the GL value for a given film.

NbN Superconducting Gap:

The superconducting gap is estimated from tunneling experiments and the Fermi velocity and can be inferred by measuring the density of conduction electrons in a Hall conductivity experiment, assuming a free electron model [45]. Scanning tunneling measurements of the gap for NbN films demonstrate that the ratio of the gap to the superconducting temperature is

reduced as the film thickness is reduced and the superconductor to insulator transition is approached [46]. Since the ratio of the gap to the T_c is fixed for a simple BCS superconductor, this is referred to as unconventional superconductivity.

Methods of Producing NbN films:

Thin films of niobium nitride have been prepared by a variety of methods, including: DC [47] and RF [41], reactive magnetron sputtering, by nitridization of niobium films during rapid thermal processing [48], chemical vapor deposition [49], and atomic layer deposition [50]. For most methods of thin film NbN deposition or growth, a greater substrate temperature results in a lower resistivity film.

Optical Properties of Sputtered NbN:

The optical properties of sputtered NbN films can vary depending on how they are deposited. In addition to the stress being greatly variable depending on the pressure, the optical reflectivity is also greatly variable [34]. While the T_c of NbN depends on the stoichiometry, the optical properties do as well. Ellipsometry was used to measure Psi and delta of thick NbN films that were deposited under a variety of conditions [51]. Here, it was noted that psi was a good indicator of the T_c as a result of the film fitting well to a simple expression for the reflectivity; the higher the $T_{c,}$ the lower was the plasma damping coefficient in a simple Drude model, with the conclusion being that the T_c decreases as the scattering from defects and disorder increases. More complex optical models have also been used [52] to describe the optical properties of NbN thin films.

References:

1. Aschermann Friedrich Justi Kramer Phys Z 42 349 1941
2. Mendelssohn, 1944 Rep. Prog. Phys. 10 358
3. Hardy, G. F., & Hulm, J. K. (1953). Superconducting Silicides and Germanides. Physical Review, 89.
4. Matthias, B. T., Gerballe, T. H., Geller, S., & Corenzwit, E. (1954). Superconductivity of Nb3Sn. Physical Review, 95(6), 1954.
5. H. Rogener Z Phys. 132 446 1952
6. Il'in, K. S., Stockhausen, a., Scheuring, a., Siegel, M., Semenov, a. D., Richter, H., & Huebers, H.-W. (2009). Technology and Performance of THz <newline/>Hot-Electron Bolometer Mixers. IEEE Transactions on Applied Superconductivity, 19(3), 269–273. doi:10.1109/TASC.2009.2018266
7. Natarajan, C. M., Tanner, M. G., & Hadfield, R. H. (2012). Superconducting nanowire single-photon detectors: physics and applications. Superconductor Science and Technology, 25(6), 063001. doi:10.1088/0953-2048/25/6/063001
8. Shoji, A., Aoyagi, M., Kosaka, S., Shinoki, F., & Hayakawa, H. (1985). Niobium nitride Josephson tunnel junctions with magnesium oxide barriers. Applied Physics Letters, 46(11), 1098. doi:10.1063/1.95774
9. Dossel, O., David, B., Fuchs, M., Kullman, W. H., & Ludeke, K.-M. (1991). A Modular Low Noise 7-Channel SQUID-Magnetometer. IEEE Transactions on Magnetics, 27(2), 2797–2800.

10. Radparvar, M., & Rylov, S. (1994). A Niobium Nitride-Based Analog to Digital Converter using Rapid Single Flux Quantum Logic Operating at 9.5K. IEEE Transactions on Applied Superconductivity, 4(2), 92–96.
11. McCaughan, A. N., & Berggren, K. K. (2014). A Superconducting-Nanowire Three-Terminal Electrothermal Device. Nano Letters, 14, 5748–5753. doi:10.1021/nl502629x
12. De Graaf, S. E., Davidovikj, D., Adamyan, a., Kubatkin, S. E., & Danilov, a. V. (2014). Galvanically split superconducting microwave resonators for introducing internal voltage bias. Applied Physics Letters, 104(5), 052601. doi:10.1063/1.4863681
13. Fabbricatore, P., Fernandes, P., Gualco, G. C., Merlo, F., Musenich, R., & Parodi, R. (1989). Study of niobium nitrides for superconducting rf cavities. Journal of Applied Physics, 66(12), 5944. doi:10.1063/1.343621
14. Pond, J. M., Carroll, K. R., & Cukauskas, E. J. (1991). Ultra-Compact Microwave Filters Using Kinetic Inductance Microstrip. IEEE Transactions on Magnetics, 27(2), 2696–2699.
15. Verkhoglyadova, T. S., L'vov, S. N., Nemchenko, V. F., Samsonov, G. V. (1967). Physical Properties of Niobium and Tantalum Nitrides. Soviet Physics Journal, 10(8), 17–19.
16. G., B. (1960). Nitrides, Carbonitrides and Oxynitrides of Niobium. Journal of the Less-Common Metals, 2, 131–137.
17. L. E. Toth, Transition Metal Carbides and Nitrides, Academic Press Inc (May 1971), ISBN-13: 978-0126959505
18. Mattheiss, L. F. (1972). Electronic Band Structure of Niobium Nitride. Physical Review B, 5(2), 315–320.

19. M. Tinkham, Introduction to Superconductivity: Second Edition, Dover Publications; Second Edition edition (June 14, 2004), ISBN-13: 978-0486435039
20. Pearl, J. (1964). Current Distribution in Superconducting Films Carrying Quantized Fluxoids. Applied Physics Letters, 5(4), 65. doi:10.1063/1.1754056
21. Gittleman, J. I., Bozowski, S., & Rosenblum, B. (1967). Transition of Type-I Superconducting Thin Films in a Perpendicular Magnetic Field: A Microwave Study. Physical Review, 161, 398–403.
22. Müller, A., Milošević, M. V., Dale, S. E. C., Engbarth, M. a., & Bending, S. J. (2012). Magnetization Measurements and Ginzburg-Landau Simulations of Micron-Size β-Tin Samples: Evidence for an Unusual Critical Behavior of Mesoscopic Type-I Superconductors. Physical Review Letters, 109(19), 197003. doi:10.1103/PhysRevLett.109.197003.
23. T. P. Orlando and K. A. Delin, Foundations of Applied Superconductivity, Prentice Hall (January 1991), ISBN-13: 978-0201183238
24. Horn and Saur, Z Phys 210 70 1968
25. Williams, M. W., Ralls, K. M., Pickus, M. R. (1967). SUPERCONDUCTIVITY OF CUBIC NIOBIUM CARBO-NITRIDES. J Phys Chem Solids, 28, 333–341.
26. Dew-Hughes, D., & Jones, R. (1980) The effect of neutron irradiation upon the superconducting critical temperature of some transition-metal carbides, nitrides, and carbonitrides. Applied Physics Letters, 36(10), 856. doi:10.1063/1.91349
27. Sadagopan, V., Gatos, H. C., Hechler, K., & Saur, E. (1969). Fast neutron damage and the current carrying capacity of niobium nitride. Z Physik, 225(3), 231–236. doi:10.1007/BF01392217

28. Storms, E. K., Giorgi, A. L., & Szklarz, E. G. (1975). ATOM VACANCIES AND THEIR EFFECTS ON THE PROPERTIES OF NbN CONTAINING CARBON, OXYGEN OR BORON--II. J Phys Chem Solids, 36.
29. Doyle N J, Hulm J K, Jones C K, Miller R C and Taylor A 1968 Phys. Lett. A 26 604
30. Mcmillan, W. L. (1967). Transition Temperature of Strong-Coupled Superconductors. Physical Review, 167(2).
31. Palanivel, B., Kalpana, G., Rajagopalan, M., & Alekseev, R. (1993). Electronic Structure and Superconductivity of NbN under High Pressure, 195.
32. Iosad, N. N., Mijiritskii, a. V., Roddatis, V. V., van der Pers, N. M., Jackson, B. D., Gao, J. R., … Klapwijk, T. M. (2000). Properties of (Nb[sub 0.35], Ti[sub 0.15])[sub x]Ni[sub 1−x] thin films deposited on silicon wafers at ambient substrate temperature. Journal of Applied Physics, 88(10), 5756. doi:10.1063/1.1319653
33. Ekin, J. W. (1982). Effect of strain on the critical current and critical field of B1 structure NbN superconductors. Applied Physics Letters, 41(10), 996. doi:10.1063/1.93369
34. Windischmann, H. (1992). Intrinsic stress in sputter-deposited thin films. Critical Reviews in Solid State and Materials Sciences, 17(6), 547–596. doi:10.1080/10408439208244586
35. Cuomo, J. J. (1982). Modification of niobium film stress by low-energy ion bombardment during deposition. Journal of Vacuum Science and Technology, 20(3), 349. doi:10.1116/1.571462
36. Kang, L., Jin, B. B., Liu, X. Y., Jia, X. Q., Chen, J., Ji, Z. M., … Wang, B. G. (2011). Suppression of superconductivity in epitaxial NbN ultrathin films. Journal of Applied Physics, 109(3), 033908. doi:10.1063/1.3518037

37. Ezaki, S., Makise, K., Shinozaki, B., Odo, T., Asano, T., Terai, H., … Wang, Z. (2012). Localization and interaction effects in ultrathin epitaxial NbN superconducting films. Journal of Physics. Condensed Matter : An Institute of Physics Journal, 24(47), 475702. doi:10.1088/0953-8984/24/47/475702
38. Komiyama, B., Wang, Z., & Tonouchi, M. (1996). Penetration depth measurements of single-crystal NbN films at millimeter-wave region. Applied Physics Letters, 68(4), 562. doi:10.1063/1.116400
39. Oates, D.E., Anderson, A.C., Chin, C.C., Derov, J.S., Dresselhaus, G., Dresselhaus, M. S. (1991). Surface impedance measurements of superconducting NbN films. Physical Review B, 43(10), 7655–7663.
40. Hossain, M.S., Yoshida, K., Kudo, K., Enpuku, K., Yamafuji, K. (1992). Enlargement of Kinetic Inductance of NbN Superconducting Thin Films for Device Applications. Jpn J Appl Phys, 31, 1033–1038.
41. Wang, Z., Kawakami, A., Uzawa, Y., & Komiyama, B. (1996). Superconducting properties and crystal structures of single-crystal niobium nitride thin films deposited at ambient substrate temperature. Journal of Applied Physics, 79(10), 7837. doi:10.1063/1.362392
42. Orlando, T., McNiff, E., Foner, S., & Beasley, M. (1979). Critical fields, Pauli paramagnetic limiting, and material parameters of Nb_{3}Sn and V_{3}Si. Physical Review B, 19(9), 4545–4561. doi:10.1103/PhysRevB.19.4545
43. Gubin, a., Il'in, K., Vitusevich, S., Siegel, M., & Klein, N. (2005). Dependence of magnetic penetration depth on the thickness of superconducting Nb thin films. Physical Review B, 72(6), 064503. doi:10.1103/PhysRevB.72.064503

44. Jesudasan, J., Mondal, M., Chand, M., Kamlapure, A., Kumar, S., Saraswat, G., … Mukhopadhyay, R. (2011). Upper Critical Field and Coherence Length of Homogenously Disordered Epitaxial 3-Dimensional NbN Films, 923(2011), 923–924. doi:10.1063/1.3606160
45. Chockalingam, S., Chand, M., Jesudasan, J., Tripathi, V., & Raychaudhuri, P. (2008). Superconducting properties and Hall effect of epitaxial NbN thin films. Physical Review B, 77(21), 214503. doi:10.1103/PhysRevB.77.214503
46. Noat, Y., Cherkez, V., Brun, C., Cren, T., Carbillet, C., Debontridder, F., … Roditchev, D. (2013). Unconventional superconductivity in ultrathin superconducting NbN films studied by scanning tunneling spectroscopy. Physical Review B, 88(1), 014503. doi:10.1103/PhysRevB.88.014503
47. Deen, M. J. (1987). The Effect of The Deposition Rate on the Properties of DC-Magnetron-Sputtered Niobium Nitride Thin Films. Thin Solid Films, 152, 535–544.
48. Brunkahl, O., Mertens, R., Bock, W., Thoma, K., & Kolbesen, B. O. (2007). Nitridation of niobium films by rapid thermal processing : different behaviour of films on oxydized silicon and monocrystalline sapphire substrates. Microchimica Acta, 156, 39–51. doi:10.1007/s00604-006-0589-7
49. Fix, R., Gordon, R., & Hoffman, D. (1993). Chemical Vapor Deposition of Vanadium, niobium, and TanTalum Nitride Thin Films. Chem. Mater., 5, 614–619.
50. Alén, P., Ritala, M., Arstila, K., Keinonen, J., & Leskelä, M. (2005). The growth and diffusion barrier properties of atomic layer deposited NbNx thin films. Thin Solid Films, 491(1-2), 235–241. doi:10.1016/j.tsf.2005.06.015

51. Tanabe, K., Asano, H., Katoh, Y., & Michikami, O. (1988). Ellipsometric and optical reflectivity studies of reactively sputtered NbN thin films. Journal of Applied Physics, 63(5), 1733. doi:10.1063/1.339910

52. Semenov, A., Günther, B., Böttger, U., Hübers, H.-W., Bartolf, H., Engel, A., … Gippius, N. (2009). Optical and transport properties of ultrathin NbN films and nanostructures. Physical Review B, 80(5), 054510. doi:10.1103/PhysRevB.80.054510

Chapter 3

Sputtering Basics:

"The plasma is like a tornado in a garbage dump"

-Professor Henry Smith.

Recounting John Coburn's description of plasmas in thin film processing, which contain a bevy of particles: electrons, neutrals, excited neutrals, positive ions, negative ions, fragments of the gas, and a variety of radicals.

The large number of inputs to the sputtering process, and the interrelation between these inputs can make it difficult to correctly interpret the results of experiments to optimize and control the properties of sputtered NbN films. For instance, a common method of optimizing the chemistry of NbN films is to vary the nitrogen flow rate between depositions, keeping all else constant, in order to measure the Tc as a function of nitrogen flow rate. However, sputtering yield and thus film deposition rate, is a function of the surface state of the sputtering target, which is itself a function of gas flow rates, target size and vacuum pumping speeds. For NbN, higher nitrogen flow rates and pressures are associated with lower sputtering yield. As a result, a plot of Tc versus nitrogen flow rate for ultrathin films will underestimate the optimal nitrogen flow because films deposited at higher nitrogen flow will be thinner and thus have a lower T_c , while films deposited at lower nitrogen flow rates will be thicker and have a higher T_c, due to size effects.

Understanding the basics of sputtering is therefore necessary in order to correctly determine how to improve and optimize ultrathin superconducting NbN films. The purpose of this chapter is to review the basics of sputtering and highlight issues relevant for the sputtering of ultrathin NbN films. We will review basic plasma physics, DC, RF and magnetron sputtering, zone growth models and stress in deposited films.

Plasma Basics:

Sputtering is a physical vapor deposition technique where ions produced in a plasma are used to bombard the surface of a metallic target in order to deposit a thin film of that metal onto a substrate. Sputtering is often used instead of other deposition methods when the desired film is a compound or alloy. For instance, evaporation of alloys can often lead to non-stoichiometric films since melting can often lead to phase separation of the constituent elements and large differences in vapor pressure can lead to films being deposited that have different composition than the source. Sputtering is one of a variety of thin film technologies that relies on plasmas.

A plasma is a fluid that contains a large number of mobile negatively and positively charged particles. A plasma can be initiated or sparked by applying a potential across a parallel plate capacitor configuration, where the space between the capacitor plates is filled with a dilute neutral gas. If the applied potential is large enough that one of the gas molecules can become ionized, the separated ion and electron will be accelerated towards opposite plates. These accelerating particles will collide with inert gas molecules at a rate determined by the mean free path in the gas, which is determined by the pressure and the scattering cross section of the gas species present. If the accelerating particles gain sufficient energy between scattering events, the

scattering can lead to ionization of additional gas. This process can lead to an avalanche, such that a significant fraction of the gas becomes ionized. The current density that results between the two plates is given by the well-known Townsend equation:

$$i = i_o \frac{e^{\alpha d}}{1 - \gamma_e (e^{\alpha d} - 1)}$$

Here, α is the probability per unit length that a collision between a gas atom and an electron will result in ionization, d is the distance between the parallel plates, and γ_e is the Townsend secondary electron emission coefficient. When positively charged gas ions strike the negative electrode surface, they have a chance to cause the emission of electrons, known as secondary electrons. The Townsend Secondary electron coefficient tells us how many secondary electrons are created per ion incident on the cathode surface. These electrons contribute to the total current between the capacitor plates and, as we'll see, the effects of secondary electrons can be more important in reactive sputtering than non-reactive.

The probability per unit length that a collision between a gas atom and an electron will result in ionization (α), depends on the ionization potential of the gas species, the mean free path in the gas, and the potential applied to the electrodes. This can be combined into an arrenhieus-like rate equation, where the ionization potential is a barrier that must be surmounted by the energy gained by the electron between scattering events:

$$\alpha = \frac{1}{\lambda} e^{\left(\frac{-V_i}{qE\lambda}\right)}$$

Where λ is the mean free path between scattering events, V_i is the ionization potential of the gas in electron volts, q is the electron charge, and E = V/d is the electric field between the capacitor plates.

Breakdown of the gas into a plasma is taken as the limit which the current goes to infinity, or equivalently, that the denominator of equation 1 goes to zero: $1 - \gamma_e(e^{\alpha d} - 1) = 0$. If we combine this with the formula for α we can get an expression for the voltage required to sustain a plasma given all of the relevant parameters, the breakdown voltage V_B:

$$V_B = \frac{\frac{V_i}{q}\left(\frac{d}{\lambda}\right)}{ln\left(\frac{d}{\lambda}\right) - ln\left(ln\left(\frac{\gamma_e + 1}{\gamma_e}\right)\right)}$$

Since the mean free path varies inversely with the system pressure P, $\lambda \propto \frac{1}{P}$, this expression for the breakdown voltage can be re-written into its better known form as Pashen's Law:

$$V_B = \frac{APd}{ln(Pd) + B}$$

where A and B are fitting coefficients that account for the relationship between the mean free path and the pressure P as well as the effect of secondary electron yield at the cathode. Paschen's Law correctly predicts that there is a minimum in the breakdown voltage versus the product of the pressure and the electrode distance. At low Pd, there are relatively few collisions between energetic electrons and gas molecules so the breakdown voltage rises. Upon increasing Pd, V_B is reduced, until the mean free path in the gas makes it such that a greater electric field is required for electrons to gain enough energy to ionize gas molecules between scattering events. Thus V_B rises with increasing Pd.

The initial stages of plasma formation is known as Townsend discharge, but once the breakdown voltage is reached and plasma becomes self-sustaining through impact ionization and secondary electron yield, we enter the normal glow regime. Here the plasma is sustained at

higher current and lower voltage and gives off a characteristic glow due to photons generated by recombining electrons and ions. During the normal glow, the current through the plasma is almost independent of the voltage. As the power through the plasma is increased, we enter the abnormal discharge regime, where current and voltage increase together. This is the regime used for sputtering. If the power is increased further, heating of the electrodes and thermionic emission will contribute to arcing and low voltage current transport.

Common laboratory plasmas, where roughly 1 in every 10,000 gas molecules is ionized, exhibit a few non-obvious behaviors related to their degree of ionization and method of creation. Laboratory plasmas are often cold or non-thermal, meaning that the electron, ion, and gas subsystems are not in thermal equilibrium. Power from the source sustaining the plasma is most effectively coupled to heating of the electrons [1]. As a result, the effective temperature of electrons in non-thermal plasmas is orders of magnitude larger than the temperature of ions or neutrals. Characteristic temperatures of electrons, ions, and neutrals in non-thermal plasmas are 20,000K, 500K and 293K respectively. The result of this is that electrons in the plasma have velocities three orders of magnitude higher than the ions do. Ions and electrons both randomly impinge on the plasma container walls, however the higher electron velocity (and lower mass / high mobility) means that surfaces immersed in the plasma receive more electron current than ion current. This causes the container to develop a potential that is lower than the bulk of the plasma, or in terms of the container being grounded, the plasma self-biases to a positive potential. This self-biasing encourages ion current and stops further charging of the chamber walls. A DC plasma will self-bias to a voltage given by the following formula:

$$V_p = \frac{k_B T_e}{q} \ln \sqrt{\frac{m_g}{2\pi m_e}}$$

Where T_e is the electron temperature in kelvin, k_b is Boltzmann's constant, m_e is the electron mass and m_g is the gas atomic mass. For the above quoted electron temperature of 20,000K with argon gas, the plasma potential is approximately 8 volts.

The transition region between the plasma and the lower potential wall (or the powered cathode) is referred to as the sheath. The sheath width is related to the Debye length, which is the screening length for isolated charge in a plasma and is given by:

$$\lambda_D = \sqrt{\frac{\varepsilon_o k_B T}{n_i q^2}}$$

The temperature T is the effective temperature of the species doing the screening, so in the case of a fixed positive charge inserted into the plasma, the screening occurs due to relatively high concentration of electrons that develop around the charge, so $T=T_e$. The density of ions is given by n_i. The sheath width can be calculated from the following expression:

$$d_s = \frac{\sqrt{2}}{3}\lambda_D\left(\frac{2q(V_p - V)}{k_B T}\right)^{\frac{3}{4}}$$

V is the voltage of the relevant surface. The sheath width is derived self consistently with the Child-Langmuir equation, which correctly predicts the current voltage relation of DC plasmas at low pressure, when the mean free path in the gas is longer than the distance between electrodes. The edge of the glowing plasma and the electrode effectively form parallel plates separated by a distance d_s. The current that flows between a powered electrode and the (negative) voltage V, is given by the CL equation:

$$\frac{I}{A} = \frac{4\varepsilon_o}{9d_s^2}\sqrt{\frac{2q}{m}}(V_p - V)^{\frac{3}{2}}$$

I is the total current, A is the electrode area, q is the electron charge and m is the mass of the charge carrier. This equation gives us the form of the IV curve in the abnormal glow regime where sputtering typically takes place. For higher pressures, when the sheath width is greater than the mean free path, a quadratic relation between current and voltage is observed: $I \propto V^2$.

DC Sputtering:

The creation of a self-sustaining plasma is typically the first step in DC sputter deposition. Consider the same parallel plate arrangement as discussed above, but now replace the cathode with a plate of some metal, which we desire to deposit in a thin film and which we will interchangeably call the target. At the anode, we place a substrate onto which we will collect the metallic film. The sputtering chamber is filled with a sputtering gas, usually argon. A plasma is established by applying DC power to the electrodes during the sparking phase. The pressure at this point is usually kept higher than the pressure used during sputtering, which shifts the sputtering gas's breakdown voltage down into a range accessible by common laboratory power supplies. This behavior can be understood through Paschen's Law. After sparking, the gas pressure is reduced and sputtering takes place at the cathode. The voltage or the current can be varied, with the other responding appropriately.

Sputtering of material from the cathode occurs in the following way. Gas molecules in the glowing region of the plasma become ionized by colliding with high-energy electrons. When these ions encounter the sheath between the plasma and the cathode, they are accelerated towards the cathode. Ions start off in the plasma at some potential V_p, are accelerated through the sheath, and arrive at the cathode at potential V (assumed to be negative), gaining energy $q(V_p\text{-}V)$. The ion impinging on the surface of the target will transfer some of this energy to target atoms at the

surface. The atomic weight of the target atoms, crystallinity of the target, total ion energy, angle of incidence, and other factors can affect what happens next, but generally some number of target atoms will be dislodged from the target surface and be sent flying into the chamber, where a portion of those atoms will collect on the substrate and become the desired thin film. The sputtering yield is defined as the number of sputtered atoms per incident ion.

Sputtering yield is affected by the details of the impinging ion and target. Generally, there is a lower threshold energy that the ion must have in order for sputtering to occur. This energy is approximately an order of magnitude greater than the heat of sublimation or surface binding energy of the target material, typically in the few to ten electron volts range [2]. At low ion energies, yield increases with increasing ion energy, approximately proportional to the square root of the ion energy (see Principles of plasma discharges…). For a wide range of elemental targets, yields are between 0.5 and 1 for 600eV argon ions [3]. Yields continue to increase until ion energies approach ~10keV. As the ion energy is increased further, yield levels off and even drops as the sputtering ions begin being implanted into the target and are unable to transfer their energy to surface atoms to help them escape the target [4]. Yield is also a function of the angle at which the ion impacts the target, roughly following $\frac{1}{\cos\theta}$ where θ is the angle between the ion velocity and the normal to the target surface. Finally, the energy distribution of material sputtered from the target is a function of the surface binding energy, with a maximum at half of the surface binding energy but is not dependent on the ion energy [1]. The energy of the sputtered material follows the Thompson formula [5]. Increasing the voltage used for sputtering can increase the yield – but the energy of the sputtered material seems to be insensitive to ion energy.

One issue with DC sputtering is the high pressure needed for reasonable deposition rates. The pressure that optimizes deposition rate in DC sputtering is on the order of 100 mtorr. At 100 mtorr, the mean free path of a particle is approximately 400μm (estimated using kinetic theory assuming argon gas, molecular diameter of 4 Angstroms, at room temperature). High pressure can lead to undesirable effects since the sputtering ions and the sputtered material may have their velocities randomized and energy lost in scattering with neutral gas. If the cathode sheath width is greater than the mean free path in the sputtering chamber, then ions will lose energy by scattering off of neutral gas on the way to the target, reducing yield. Similarly, sputtered material will also lose energy and move more diffusively about the sputtering chamber. This result can contribute to less ideal film morphology as well as reduced deposition rates due to material diffusing away from the substrate. Lastly, the higher the pressure during deposition, the more sputtering gas impinges on the surface of the depositing film, and the more gas is incorporated into the final product.

Reducing the pressure during DC sputtering will alter the plasma dependent on how it is being powered. If the voltage is being held constant, the current will drop when the pressure is reduced, because for a fixed accelerating voltage there are fewer interactions between electrons and neutral atoms leading to ions and electrons for conduction. The reduced current will result in reduced deposition rates. On the other hand, if the current is fixed, then the voltage will rise to accommodate the reduced probability of electron neutral interaction. DC sputtering below 30 mtorr is not usually feasible [6].

Magnetron Sputtering:

In order to address the high pressure required for DC sputtering, magnetron sputtering was developed. In magnetron sputtering, a magnetic field is applied that is perpendicular to the electric field between the cathode and anode. Due to these perpendicular fields, electrons that would otherwise simply accelerate towards the anode execute cycloid motion, with the net motion perpendicular to both fields. This increases the likelihood of impact ionization by effectively trapping the electron near the cathode. The result is that at a given pressure and target voltage, greater current density flows between the electrodes. Alternatively, magnetron sputtering allows the same current to flow at lower gas pressures. DC magnetron sputtering at a few mtorr allows sputtered material to arrive at the substrate with more of its initial energy.

The IV curve of a DC magnetron sputtering source has been proposed to have the following form [7]:

$$I = \beta(V - V_o)^2$$

V_o is the minimum voltage for maintaining the discharge. In order for the glow discharge to be self-sustaining, every electron emitted from the cathode must produce sufficient ions to create one additional electron at the cathode. This minimum voltage is given by the expression:

$$V_o = \frac{kV_i}{\Gamma_e \varepsilon_i \varepsilon_e}$$

V_i is the ionization energy of the sputtering gas, Γ_e is the effective secondary electron yield, ε_i is the ion collection efficiency, and ε_e is the ion generation efficiency [8]. k may be regarded as a fitting constant.

Due to the magnetron, the secondary electron yield from the target is effectively reduced, since secondary electrons captured in the magnetron have a pressure-dependent chance of being recaptured by the cathode, unlike without the magnetron [9]. At sufficiently low pressure, the

cycloid motion of a free electron that starts at the cathode surface with zero velocity will cause the electron to return to the cathode surface where it can be recaptured. Without the magnetron it would move towards the anode unambiguously. The reduced effective secondary electron yield is clearly compensated for by the increased number of ions produced per secondary, due to the increased plasma densities and deposition rates made possible by magnetrons. This result does suggest however that a sufficiently strong magnetic field could actually increase the plasma impedance.

The value of β is correlated with the strength of the magnetic field of the magnetron and is roughly a measure of the magnetron efficiency. β changes with pressure depending on the magnetic field strength and changes with secondary electron yield [7].

Other workers have put forth different dependencies of the current on the voltage and noted that the increased ejection of high-energy material from the cathode can change the local gas density at the cathode [10]. They note that the IV relation in DC magnetron sputtering is generally $I \propto V^n$, but n is a function of sputtering gas type, pressure, and target material.

While most of our above discussion has assumed that the anode and cathode have a parallel plate geometry, many sputtering tools employ the sputtering gun geometry, which is slightly more complicated but should not materially affect the present discussion. The design of the magnetron and the shape of its field has received due attention, for instance in the design of unbalanced magnetrons which promote bombardment of the growing film. One substantial issue in magnetron sputter guns is target erosion. As the target gets thinner, the magnetron trap is effectively strengthened, since the permanent magnets which form the magnetron are located behind the target. This causes the sputtering voltage to drop over time if the current is held constant because the increased confinement leads to fewer electrons lost from the plasma and

greater ionization [11]. This was tested more directly in ref [7] where the target was composed of a stack of 1 mm thick Cu targets in the same magnetron. By progressively removing targets, the voltage dropped by 50% with current and pressure being kept constant.

Other Sputtering Considerations:

One of the reasons sputtering is frequently used to deposit alloy films is that unlike other deposition mechanisms, the deposited film will have the same stoichiometry as the target. During sputtering the bulk of the source material remains solid, and limited amounts of diffusion occur at the surface. Also, the sputtering yields for different elements for the same ion energy and conditions are usually not too different, but in extreme cases may vary by 100%. When sputtering from an alloy target, the material with higher yield will sputter more readily, but this causes a form of negative feedback. The surface becomes enriched in the low yield material, and equilibrium is reached when the surface state has shifted so that the sputtered material has the stoichiometry of the original target. This stands in stark contrast to evaporation, where alloy melts change in stoichiometry continuously due to large differences in evaporation rates of different metals without corresponding negative feedback.

During sputter deposition, the following cause the substrate to heat: bombardment by all gaseous species including the sputtered material, electrons, ions, and neutral atoms reflected from the cathode and the heat of condensation released by sputtered material that incorporates into the film. We can estimate the maximum rise in the substrate temperature due to each of these effects by ignoring any heat loss mechanisms such as heat conduction through the substrate holder or radiation. During deposition this will then give the following:

$$T(t) = 2.67 \times 10^{-29} \frac{\dot{d}\left(H_c + E_k + E_p\right)}{\rho c d \Omega} t$$

Where H_c, E_k and E_p are the heat of condensation, kinetic energy of the deposit, and average kinetic energy of all other bombarding species from the plasma, each in eV/atom. $\dot{d}$ is the deposition rate in angstroms per minute. ρ, c, d, and Ω are the film density in g/cm^3, the heat capacity in J/gC, the substrate thickness in cm, and the volume per atom of the sputtered material in cm^3/atom. Ref [12] discusses substrate heating further and contains relevant numbers for a range of target materials. Using the above formula for an aluminum target, with a deposition rate of 1000nm/min on a standard 500um thick silicon substrate, the maximum temperature increase is around 150C after 60 seconds. Note that the addition of substrate biasing can substantially increase the E_p term.

RF Sputtering

All of our preceding discussion has assumed that it is possible to drive a DC current through the target material. This is true for metallic targets, but if we want to sputter some type of insulator, we cannot practically use direct current; driving 100mA through a SiO2 target (circular with a diameter of 2 inches and a thickness of 0.25 inches) would require more than 10^{15} volts.

In order to sputter from insulating targets, RF sputtering must be used, although it is not entirely obvious how RF sputtering works. A common misconception is that RF sputtering works like DC sputtering, and that every half cycle sputtering occurs at the cathode and on the other half at the anode. For simplicity, let's once again imagine a parallel plate configuration, where

one of the plates is made from a material that we wish to sputter. The electrodes are immersed in a dilute gas.

First, a plasma must be sparked, similar to a DC plasma, which requires that a few electrons and ions, formed spontaneously or via the absorption of an energetic particle, gain enough energy to cause further ionization and precipitate an avalanche process. A zeroth order approximation of how an RF source can spark a plasma is to estimate the energy gained by an electron in an oscillating field and equate that with the ionization potential of the gas. Calculating the maximum kinetic energy of a free electron in an electric field of strength E with angular frequency ω yields: $E_k = (qE)^2/(2m_e\omega^2)$. Assuming the frequency is 13.56 MHz (a radio band reserved by the FCC for scientific and industrial equipment), the electron energy will equal the energy needed to ionize argon when the electric field is ~11.5V/cm. Although this analysis ignores scattering of the electrons before reaching this energy, it turns out that RF fields are more efficient at transferring energy into the electron system, and as a result plasmas spark readily.

Once the plasma is established, as in the case of the DC discharge, the plasma will self-bias to a potential slightly higher than those of the electrodes/chamber walls. This potential is on the order of 10 Volts, not enough to cause sputtering, and as in the DC case, this is due to the high mobility of the electrons far exceeding that of the ions. Fast-moving electrons bombard surfaces exposed to the plasma until the potential of those surfaces has fallen enough that the induced ion current stops further charging.

A DC voltage large enough to give ions enough energy to cause sputtering is induced by the application of an RF potential. Assume that a plasma exists between the electrodes, one of which is the target. When the potential at the target is positive, it draws electrons towards it easily due to their high mobility. On the other half cycle however, it collects very few ions. The

result is that the target builds up a negative DC voltage that encourages ion current. In steady state, the DC voltage of the target drops until the number of ions and the number of electrons collected each cycle is equal. This equality can be used to determine the amount of time that the total potential (RF+DC) of the target spends above zero volts, if we know the electron and ion velocities and secondary electron yield. The result is that the total potential is positive for about 0.1% of each cycle. Another way to look at this is to make the approximation that $V_{DC} = -V_{RF}$, where V_{RF} is the amplitude of the applied RF signal (with peak to peak voltage of $2V_{RF}$).

All of the above arguments for how the target builds up a negative DC voltage also work for the other electrode. A DC voltage will develop between it and the plasma to balance ion and electron currents, and if the voltage is sufficiently large, sputtering will occur. Sputtering from anything other than the target can be a major source of contamination.

Sputtering from only the target in an RF plasma can be ensured by making the surface area of the target sufficiently smaller than that of the other electrode. This is not difficult, since in most deposition chambers, the other electrode is tied to the chamber wall and to ground. In order to see how this is possible, we can model the plasma between the electrodes as series capacitors, where one capacitance is between the target and the plasma glow region, and the other capacitance is between the glow and the counter electrode. Each capacitor is proportional to the electrode area, and inversely proportional to the sheath widths between each electrode and the plasma. If we apply an RF voltage across these series capacitors, we can determine the ratio of the voltages that drop across each sheath:

$$\frac{V_{target}}{V_{other}} = \frac{C_{other}}{C_{target}} = \frac{A_{other}d_{target}}{A_{target}d_{other}}$$

where Vi, Ci, Ai, and di are the voltage, capacitance, electrode area and sheath width for the appropriate electrode. We can now use Child's law to relate the voltage across each sheath, to its width. As a reminder, Child's law relates the current density to the voltage across parallel plate electrodes with a collisionless (mean free path greater than d_s) discharge in between:

$$\frac{I}{A} = \frac{4\varepsilon_o}{9d_s^2}\sqrt{\frac{2q}{m}}V^{\frac{3}{2}}$$

If we rearrange this we get:

$$d_i = c\sqrt{\frac{A_i}{I}}V_i^{\frac{3}{4}}$$

where c combines all of the constants in Childs law not relevant to the present discussion. A_i is the area of the electrode and I is the total current flowing between the electrode and the plasma, and V_i is the voltage across the sheath. The ratio of the target sheath to the other sheath is:

$$\frac{d_t}{d_o} = \sqrt{\frac{A_t}{A_o}}\left(\frac{V_t}{V_o}\right)^{\frac{3}{4}}$$

We can now plug this into our earlier relation for V_t/V_o:

$$\frac{V_t}{V_o} = \frac{A_o}{A_t}\sqrt{\frac{A_t}{A_o}}\left(\frac{V_t}{V_o}\right)^{\frac{3}{4}} = \sqrt{\frac{A_o}{A_t}}\left(\frac{V_t}{V_o}\right)^{\frac{3}{4}}$$

Finally we get:

$$\frac{V_t}{V_o} = \left(\frac{A_o}{A_t}\right)^2$$

when $A_o >> A_t$, $V_t >> V_o$. In other words, the majority of the RF potential drops across the target sheath. The DC voltage bias develops at the target and the other electrode in accordance with our discussion on self-biasing due to the electron mobility being much greater than the ion mobility, however the bias voltage at the counter electrode should be low enough that effectively no sputtering occurs.

Note that the above relationship, $\frac{V_t}{V_o} = \left(\frac{A_o}{A_t}\right)^2$, is not what you will find in textbooks. No less than two texts ([13] and [1]) state the relationship as $\frac{V_t}{V_o} = \left(\frac{A_o}{A_t}\right)^4$. However, the derivation in [13] assumes that the current density at each electrode is constant. This seems like a bad assumption when we are also assuming that one of the electrodes is significantly larger than the other. It implies that one electrode is drawing significantly more current, despite being connected in series with the other. By assuming that the total current is equal I get the quadratic expression. There may be something to this, where, as reference [1] points out on page 432, the experimentally relationship appears to be close to $\frac{V_t}{V_o} = \left(\frac{A_o}{A_t}\right)^n$ with $n \lesssim 2.5$. While he proposes a solution, it relies on assuming collisions in the sheath – a regime that is not valid if Child's law is used.

Once the DC bias is established due to the application of RF power, our knowledge of DC sputtering can be applied.

Reactive Sputtering

Creating a compound target of high purity with a desired stoichiometry is a difficult task. As a result, it is often easier to sputter from a metallic target, while fostering the conditions necessary

for the desired compound to form at the surface of the target, in the plasma, and on the depositing film, resulting in a compound film of high purity. This is the basis of reactive sputtering, and causing the reaction is usually as simple as flowing a reactive gas into the chamber while sputtering. However the chamber conditions, as complex as they can be from simply maintaining a plasma, are made more complex by the reactive gas.

The central difficulty with reactive sputtering is balancing hysteretic IV behavior, film stoichiometry, and deposition rates, which are all affected by the flow of reactive gas. Compounds that can be formed with reactive sputtering, including a variety of oxides, nitrides, carbides, sulfides and combinations thereof, generally have different secondary electron emission coefficients and different sputtering yields than their metallic constituents. As we have seen, the secondary electron yield has a dramatic effect on the plasma behavior. It is not hard to imagine that the current-voltage behavior of a plasma can be very different based on the details of the reactive gas pressure, flow, and history.

Hysteresis in reactive sputtering can be understood in the following way. Assume that we start in a state where there is no compound on the target surface, but we have established a plasma and sputtering and we are holding the voltage constant. As we begin the flow of reactive gas, compound will form at the target surface, but relatively little gas will fill the chamber. Assuming that the compound has a lower secondary electron emission coefficient, the current will fall, which can be seen as an increase in the plasma impedance due to the lower secondary yield. This reduction in current means that fewer ions reach the surface and cause sputtering relative to the number of reactive gas molecules that reach the target and form the compound. As the flow rate of the reactive gas is increased, the target surface becomes increasingly covered by the compound, until at some flow rate the positive feedback described above (lower secondary

yield → lower current → fewer ions per gas molecule) results in a large drop in current and a target surface that is almost fully covered in the compound. This drop in the current is accompanied by a rise in the reactive gas pressure in the chamber, since it is no longer being fully consumed by the target. At this point, when the flow rate of reactive gas is reduced, a much lower gas flow rate is needed before the plasma switches back to the original high current regime, since an over pressure of the reactive gas exists to maintain a poisoned target. Similar hysteretic behavior can be observed when the current is held fixed and the reactive gas flow is changed. The IV curve in such a system has a characteristic ‘S’ shape that can be fully traversed in current control mode, but remains hysteretic in voltage control mode.

An important thing to keep in mind with reactive sputtering is that the reactive gas flow rate does not determine the pressure of the reactive gas in the chamber. This is because the reactive gas is consumed by the target and the film. This result should make it clear that the deposition rate is changed by the flow of reactive gas, both by changing the sputter yield at the target, and by encouraging more or less compound to form at the target.

Berg’s model is a simple analytical model that can be used to understand the effects of a wide range of process variables that determine reactive sputtering results [14]. The main result of Berg’s model is the prediction of hysteretic effects in reactive sputtering due to the nonlinear relation between reactive gas flow rate and reactive gas pressure, as well as conditions under which hysteresis can be reduced or eliminated. The model has been used to predict that the following factors can affect hysteresis: target material, type of reactive gas, vacuum pumping speed, and the sizes of both the target and the total collecting area (some small percentage of which will be the substrate).

According to Berg's model, hysteresis can be eliminated if the pumping speed of the vacuum is sufficiently high [15]. For a given material system and deposition chamber, it is likely that pumping speed is the only possible remedy for hysteresis since all of the other factors are likely fixed, but many deposition chambers allow throttling of the vacuum. Unfortunately, the maximum pumping speed is fixed by the pump, so this option is only available if the vacuum was being throttled or is inefficiently coupled to the chamber. Increasing the pump speed can eliminate hysteresis because a sufficiently high vacuum speed causes the total reactive gas consumption to be monotonic with gas pressure.

Improvements on Berg's model have been implemented. Berg recently published work on adding the effect of ionized reactive gas implantation in the target and sputtering of compounds as separate species [16]. Another model added the effect of secondary electron emission of both the target material and the compound [17].

Experimental work has been done to show that the effective secondary electron yield of a target is an average of the secondary electron yield of the component materials of the target, weighted by the area of those materials [18]. These experiments where done with a target made up of wedges of copper and aluminum, assembled in different areal ratios, and it was shown that the secondary electron yield followed the expression:

$$\gamma_e = \gamma_{Cu}\theta_{Cu} + \gamma_{Al}(1 - \theta_{Cu})$$

where γ_{Cu} is the secondary electron yield of copper, γ_{Al} is the secondary electron yield of aluminum, and θ_{Cu} is the fraction of the total target area that was copper, with the remainder made up of aluminum. This appears to be true for targets that are partially covered in compound during reactive sputtering as well and can explain well known increases or decreases in discharge

voltage depending on the state of the target surface [19]. Reference [19] also gives expressions for the secondary electron yield as a function of the ion energy and metal work function, a consideration not frequently mentioned.

Structure-Zone Models

In order to understand and classify film morphologies that are observed from sputter deposited films in varying conditions, a variety of models have been developed. The zone structure model of Thornton [20] attempts to delineate film morphologies as a function of the homologous temperature and the sputtering pressure. The homologous temperature is the temperature of the substrate divided by the melting temperature of the film being deposited.

Thornton's model classifies films into four different categories or zones, based on the dominant mechanism growth mechanism. The first zone is dominated by shadowing effects and is roughly what is expected at low temperatures and high pressures. Material that arrives at the surface of the film sticks wherever it first lands. High points in the film tend to collect more material than low points because the material flux arrives at the surface at oblique angles due to scattering off of gas. This leads to columnar grains, anisotropic structures, and voids. At higher temperature, zone two is defined by surface diffusion effects. Sputtered material that arrives at the surface of the film can move until it is incorporated. Grains are larger and voids are absent. Finally, zone three is defined by high homologous temperature and bulk diffusion in the film. Grains are larger and equiaxed. Thornton's main contribution was to recognize a transition zone between zones one and two. At low temperature, when the material flux is normal to the substrate surface, a film will form that is denser and not voided compared to the zone one film.

The transition zone may be thought of roughly as the zone of low homologous temperature and low pressure.

Without recourse to the deposition specifics, we can describe the various zones in the following way. Zone one structure is dominated by the transport of the sputtered material to the surface. Zone two structure is determined by surface diffusion, and zone three is dominated by bulk diffusion. The transition zone between one and two is due to the increased surface diffusion arising from various effects. Transition zone films are considered to be made up of the same kind of material as zone one, but denser and without voids.

Other structure zone models have been proposed as well. Messier's revised structure zone model replaces the pressure axis of Thornton with the net bombardment energy form sputtered material, reflected neutrals and ion bombardment [21]. Messier argues that this is a more fundamental model, since the bombardment energy encompasses the effects of higher pressure, but also allows for considerations like intentional bombardment. Recently, yet another extension of Thornton's model was proposed, wherein the axes considered are the effective temperature, the kinetic energy of bombarding particles, and thickness [22]. The effective temperature is the homologous temperature plus an increase in temperature due to potential energy sources including the heat of sublimation and heat released by ions joining the film and capturing electrons. The kinetic energy axis is as it was in Messier's model, while the thickness axis accounts for resputtering from the film.

Stress in Sputtered Films

An important issue in sputter deposition of thin films is the stress that can develop within the film as a result of the deposition specifics. Intrinsic stress in sputtered films can be either tensile or compressive depending on the deposition parameters. In metallic films there is an association between tensile stress and zone one microstructures, and between compressive stress and transition zone microstructure [20]. Films whose intrinsic stress is tensile tend to have higher resistivity and lower optical reflectivity when compared to films with compressive stress.

A universal feature of intrinsic stress in thin metallic films is the transition from tensile stress when deposited at high pressure (~30 mtorr), to compressive stress when deposited at low pressures (~1 mtorr), along with a transition from low reflectivity to high reflectivity [23]. This behavior is explained by the bombardment the growing film receives from ions that capture electrons at the target and are reflected with a high percentage of their initial energy towards the film. This energetic bombardment mechanism is supported in at least two ways. By changing the sputtering gas species it is observed that heavier sputtering gases induce the stress transition in sputtered films at higher pressure for the same target material. Reflected neutral heavy gas molecules arrive at the film surface with greater momentum than lighter sputtering gases, at the same pressure and sputtering voltage. Additionally, by changing the target material with the same sputtering gas, it is observed that the stress transition pressure is linear with the target atomic mass. Impinging ions are more likely to be reflected by heavier target atoms, leading to greater bombardment.

While the stress transition at low temperature is universal, the intrinsic film stress is a more complex function of bombardment energy. As Thornton alludes to, and recent work inspiring Messier's and Ander's structure zone models indicate, it is often necessary to include the effects of all sources of energy that deposit on the developing film, including the kinetic

energy of the deposit material itself. In fact, once the bombardment energy is high enough, plastic deformation of the film can occur, reducing the compressive stress [24]. Lastly, none of these captures the effect on entrapped gas. The amount of sputtering gas that becomes entrapped in the deposited film produces additional stress mechanisms.

A variety of different models have been proposed to explain intrinsic stress. A thorough review by Windischmann details some of these theories, in addition to everything else related to stress in sputtered films [24]. Ohring's text (ref [13]), section 12.5.5, also gives a good overview of possible origins of intrinsic stress.

An additional mechanism that produces stress in thin films is mismatch between the coefficient of thermal expansion of the film and the substrate. When films are deposited at elevated temperature and then used at lower temperature this stress is typically tensile and can be substantial. In the limit that the substrate is much thicker than the film, the thermal stress is:

$$\sigma(T) = \frac{(\alpha_s - \alpha_f)(T - T_d)Y_f}{1 - v_f}$$

Here, α is the coefficient of thermal expansion of the film or substrate, T_d is the temperature of the film and substrate during deposition, Y_f is the young's modulus of the film, v_f is the Poisson's ration of the film, and T is the temperature. If $T_d > T$, and $\alpha_s > \alpha_f$, this formula predicts a positive, tensile stress in the film. This is usually the case for thin metal films on insulating substrates. The total stress in the film is the sum of the intrinsic stress and this thermal stress.

Intrinsic stress itself is a function of substrate temperature during the deposition. As the homologous temperature is increased, the characteristic curve for stress reversal shifts to lower

bombardment energy [25]. The maximum stress in the film is reduced, as we would expect in an unstressed film at high temperature.

Bias Sputtering:

Bias sputtering is sputter deposition where the substrate is held at a negative voltage to promote ion bombardment. The bias can be applied as a DC or an RF signal, with the net result being an increased difference between the plasma voltage and the substrate voltage. Ions are accelerated across the resultant sheath, gaining energy proportional to the bias voltage. Ions bombarding the surface of the film lead to a variety of effects. Ion bombardment has been shown to affect the following properties of sputter deposited films: grain size, intrinsic stress, crystallographic orientation, resistivity, reflectivity, effective deposition temperature, surface roughness, adhesion, defects, and film density.

The effect of bias sputtering can be best understood in the case of adding bias sputtering to a film at low homologous temperature that would otherwise develop a type one film structure. Such films have voids and sparse columnar grains as a result of being dominated by shadowing effects. In exactly the same way that high points in films like this tend to receive more material flux, the addition of the film bias means that high points in the film are likely to be struck by an energetic ion. This can cause sputtering away from the film, or forward sputtering where dislodged material is moved into voided or sparse regions. Thus, the addition of substrate bias helps transform type one films into transition-type films, which tend to have a host of improved properties.

It has been shown that the amount of sputtering gas trapped in the bias sputtered films of amorphous metal alloys is proportional to the bias voltage squared [26].

Conclusions:

The plasma environment used in sputter deposition is complex, and many if not all of the expressions stated above are greatly simplified. Most of the important parameters used to describe the plasma, such as the secondary electron yield, are not constant, but rather, are functions of some other plasma variable. The secondary electron yield is a function of the ion energy, which is a function of the sheath voltage, which is related to the plasma impedance and the secondary electron yield. Of course, determining what matters in a given scenario is necessary and simplifying assumptions will have to be made.

References:

1. M. A. Lieberman and A. J. Lichtenberg, Principles of Plasma Discharges and Material Processing, second edition, Wiley-Interscience, 2005.
2. Malherbe, J. B. (1994). Sputtering of compound semiconductor surfaces. I. Ion-solid interactions and sputtering yields. Critical Reviews in Solid State and Materials Sciences, 19(2), 55–127. doi:10.1080/10408439408244588
3. Laegreid, N., & Wehner, G. K. (1961). Sputtering Yields of Metals for Ar+ and Ne+ Ions with Energies from 50 to 600 ev. Journal of Applied Physics, 32(3), 365. doi:10.1063/1.1736012

4. Mahan, J. E., & Vantomme, A. (1997). A simplified collisional model of sputtering in the linear cascade regime. Journal of Vacuum Science & Technology A: Vacuum, Surfaces, and Films, 15(4), 1976–1989. doi:10.1116/1.580668
5. D. Depla, S. Mahieu (Eds.), Reactive Sputter Deposition, Springer, Berlin, 2008
6. J. L. Vossen and W. Kern, Thin Film Processes, Academic Press 1978, ISBN-13: 978-0123960276
7. Depla, D., Buyle, G., Haemers, J., & De Gryse, R. (2006). Discharge voltage measurements during magnetron sputtering. Surface and Coatings Technology, 200(14-15), 4329–4338. doi:10.1016/j.surfcoat.2005.02.166
8. Thornton, J. a. (1978). Magnetron sputtering: basic physics and application to cylindrical magnetrons. Journal of Vacuum Science and Technology, 15(2), 171. doi:10.1116/1.569448
9. Buyle, G., De Bosscher, W., Depla, D., Eufinger, K., Haemers, J., & De Gryse, R. (2003). Recapture of secondary electrons by the target in a DC planar magnetron discharge. Vacuum, 70(1), 29–35. doi:10.1016/S0042-207X(02)00664-4
10. Rossnagel, S. M., & Kaufman, H. R. (1988). Current–voltage relations in magnetrons. Journal of Vacuum Science & Technology A, 6(2), 223. doi:10.1116/1.574985
11. Depla, D., Strijckmans, K., & De Gryse, R. (2014). The role of the erosion groove during reactive sputter deposition. Surface and Coatings Technology, 258, 1011–1015. doi:10.1016/j.surfcoat.2014.07.038
12. Thornton, J. a. (1978). Substrate heating in cylindrical magnetron sputtering sources. Thin Solid Films, 54(1), 23–31. doi:10.1016/0040-6090(78)90273-0
13. M. Ohring, Materials Science of Thin Films, Second Edition, Academic Press, 2001, ISBN-13: 978-0125249751

14. Berg, S., & Nyberg, T. (2005). Fundamental understanding and modeling of reactive sputtering processes. Thin Solid Films, 476(2), 215–230. doi:10.1016/j.tsf.2004.10.051

15. Nyberg, T., Berg, S., Helmersson, U., & Hartig, K. (2005). Eliminating the hysteresis effect for reactive sputtering processes. Applied Physics Letters, 86(16), 164106. doi:10.1063/1.1906333

16. Berg, S., Särhammar, E., & Nyberg, T. (2014). Upgrading the "Berg-model" for reactive sputtering processes. Thin Solid Films, 565, 186–192. doi:10.1016/j.tsf.2014.02.063

17. Matsuda, Y., Otomo, K., & Fujiyama, H. (2001). Quantitative modeling of reactive sputtering process for MgO thin film deposition. Thin Solid Films, 390(1-2), 59–63. doi:10.1016/S0040-6090(01)00925-7

18. Depla, D., Tomaszewski, H., Buyle, G., & De Gryse, R. (2006). Influence of the target composition on the discharge voltage during magnetron sputtering. Surface and Coatings Technology, 201(3-4), 848–854. doi:10.1016/j.surfcoat.2005.12.047

19. Depla, D., Mahieu, S., & De Gryse, R. (2009). Magnetron sputter deposition: Linking discharge voltage with target properties. Thin Solid Films, 517(9), 2825–2839. doi:10.1016/j.tsf.2008.11.108

20. Thornton, J. a. (1986). The microstructure of sputter-deposited coatings. Journal of Vacuum Science & Technology A: Vacuum, Surfaces, and Films, 4(6), 3059. doi:10.1116/1.573628

21. Messier, R. (1984). Revised structure zone model for thin film physical structure. Journal of Vacuum Science & Technology A: Vacuum, Surfaces, and Films, 2(2), 500. doi:10.1116/1.572604

22. Anders, A. (2010). A structure zone diagram including plasma-based deposition and ion etching. Thin Solid Films, 518(15), 4087–4090. doi:10.1016/j.tsf.2009.10.145

23. Hoffman, D. W. (1994). Perspective on stresses in magnetron-sputtered thin films. Journal of Vacuum Science & Technology A: Vacuum, Surfaces, and Films, 12(4), 953. doi:10.1116/1.579073

24. Windischmann, H. (1992). Intrinsic stress in sputter-deposited thin films. Critical Reviews in Solid State and Materials Sciences, 17(6), 547–596. doi:10.1080/10408439208244586

25. Roy, R. A., Petkie, R., & Boulding, A. (1991). Properties and microstructure of tungsten films deposited by ion-assisted evaporation. J Mater Res, 6(1).

26. Cuomo, J. J., & Gambino, R. J. (1977). Incorporation of rare gases in sputtered amorphous metal films. Journal of Vacuum Science and Technology, 152(1977). doi:10.1116/1.569109

Chapter 4

Methods:

Accurate determination of the properties of few-nanometer-thick superconducting films is an essential part of establishing a material system for device fabrication or for fundamental studies of the properties of thin film superconductors. This chapter details the methods and equipment used to deposit and characterize ultrathin niobium nitride films that are examined in this work. Films approximately 4nm thick were deposited by reactive DC magnetron sputtering varying the sputtering pressure, process gas flow rates and substrate temperature and conditions. Sheet resistance, superconducting critical temperature, and thickness were measured on almost all films produced. Some films were measured using x-ray reflectivity as a way to determine thickness and gain some information about film density. These methods can be directly applied to other thin metallic films and superconductors.

Substrate Preparation:

Substrate preparation and cleanliness have a large impact on the material properties of films that are only a few nanometers thick. The substrate should be free of hydrocarbons and other adsorbed materials that can interfere with the deposited film by affecting morphology or

contributing to impurities. Substrate roughness must be substantially less than the intended thickness of the film otherwise film continuity may not be possible.

Silicon dioxide (SiO_2) and silicon nitride (SiN_x) thick films were prepared by thermal oxidation or low pressure chemical vapor deposition (LPCVD) on 100 mm diameter, 500 micrometer thick, boron doped, <100> orientation, double side polished silicon wafers. The supplier, Silicon Valley Microelectronics, provided the following information about the wafers used in this work: roughness less than 2 angstroms, resistivity between 11 and 16 Ohm-centimeters, total thickness variation less than 9.3 micrometers, bow of -3.4 to 4.4 micrometers and warp of 3.8 to 11.6 micrometers. Thermal oxide was grown to a thickness of 255 nm, while the deposited nitride was 172 nm. Each of these thicknesses on silicon form antireflection coatings for 1550 nm light and were useful for efficient coupling of light to devices patterned out of the NbN.

One centimeter square samples were prepared for deposition by die sawing the prepared oxide and nitride wafers. Four inch wafers of SiO_2 or SiN_x were first spin coated with S1813 photo-resist at a speed of 3000 rotations per minute for 60 seconds, and then baked at 85 °C for three minutes to drive off solvents. These photoresist protected wafers were then cut into 1 cm by 1 cm samples by a die saw in a shared circuit packaging area. Cuts were aligned to the flat of the wafer such that the silicon crystal orientation of each sample could later be determined if necessary. Each sample was marked with a small arrow scratched into a corner on the backside of the sample with a diamond scribe, with the arrow head pointing towards the direction of the wafer flat. This arrow also served to distinguish which side of the sample was the back and which was the front, the front being the side where the NbN would eventually be deposited. In the case of the thermal oxide, the front was simply chosen as the side with less particulates on

the surface before dicing. In the case of the nitride, the front was taken as the side that was face down in the vertical tube reactor during the LPCVD.

Samples were cleaned with solvents and with a 100W oxygen plasma before deposition. Samples were sonicated in acetone for three minutes at maximum power to remove the photoresist, then spray cleaned with acetone, methanol and isopropyl alcohol before being blown dry with nitrogen gas. Samples were then placed inside of a vacuum chamber where a 100W oxygen plasma was ignited to clean off any remaining organic materials from the surface. The plasma was maintained for 3 minutes. Samples cleaned in this way were then stored inside of a nitrogen dry box and used as needed. The storage time varied between less than an hour and weeks.

DC Reactive Magnetron Sputtering:

Films were deposited by DC reactive magnetron sputtering inside of an AJA Inc ATC Orion sputtering system. The system is equipped with a load lock and maintained at a base pressure of approximately 5×10^{-9} torr by an Oxford Instruments CryoPlex 8 cryopump, with a pumping speed of 1500/4000/2500/1200 liters per second of air/water/Hydrogen/Argon and an unmeasured ultimate pressure. The load lock was used to ensure that the system could be kept at high vacuum without interruption for loading samples into the chamber, thus minimizing the presence of residual gases during deposition. The loadlock was pumped by a Pfeiffer model TMH071P turbomulecular pump with pumping speed 60 liters per second of nitrogen and an ultimate vacuum of less than 7.5×10^{-7} torr. The chamber was equipped with two 1000W halogen heat lamps which were used to heat the substrate holder and substrates to a maximum of

800 °C during deposition. A two inch diameter, ¼ inch thick 99.95% niobium target from Kurt J Lesker was used inside of a shuttered magnetron sputtering gun. Argon was flown into the source, while nitrogen was flown into the chamber near the substrates. The flow rate of each gas was controlled by mass flow controllers manufactured by MKS Instruments. The base pressure of the system was monitored by an ion gauge manufactured by Granville Phillips, model 274, while the pressure during the deposition was monitored by a capacitive manometer.

The process for depositing NbN films followed this general procedure. Cleaned substrates were loaded into shallow pockets in an Inconel substrate holder, and held in place by a thin Inconel plate. The plate both held the samples in place, and openings in the plate defined the areal shape of the resulting film, acting as a shadow mask. The plate was fixed in place by 12 stainless steel screws. Once the samples were loaded into the holder and the mask was screwed down, the surface was blown with ultra high purity helium to dislodge any dust or particulate that had developed during the loading process. This gas was used for convenience and could be replaced with nitrogen. The substrate holder was then placed face down into the loadlock, onto the transfer arm. The loadlock was then closed and pumped down for approximately 20 minutes. After the loadlock was pumped down, the substrate holder was transferred to the column connected to the heater assembly. The transfer arm was withdrawn, gate valve closed, and the substrate holder and heater assembly was lowered into place above the sputtering source before being rotated at a speed of one revolution every three seconds. Argon was then flown into the sputtering source, while nitrogen was flown into the chamber near the substrate holder. The flow rates were controlled by flow controllers. The system pressure was maintained by an automated gate valve that throttled the cryopump. Argon was flowed into the system at a rate of 26.5sccm to a pressure of 30mtorr. At these settings, a pre-deposition test spark of the plasma was run to

test whether the system was operating as normal, as judged by the voltage that developed across the source. The DC power supply was turned on in current control mode to 400mA, and the resulting power dissipated at the source was recorded. Once this was done, the power supply and argon flow was turned off and the cryopump gate valve was fully opened to reduce the system pressure. At this point, the substrate heaters were turned on and the substrate was heated to 800 °C in vacuum. The temperature of the substrate holder was inferred by a thermocouple located inside of the heater assembly. The mapping of the thermo couple temperature to the temperature of the substrate holder was done at the manufacturer. Once the substrate holder reached 800 °C, the temperature was maintained at this level for an additional 20 minutes. The ion gauge pressure after 20 minutes of heating at 800C was roughly 2E-8 torr.

The deposition took place after the 20 minute heat soak. First argon was flown into the system at a rate of 26.5 sccm to a system pressure of 30mtorr. At this point the DC powerssupply connected to the source containing the Nb target was turned on to spark the plasma. Once the plasma was initiated, the pressure was reduced by opening the cryopump gate-valve (done automatically), to 2.5 mtorr. At this pressure, the mean free path of gas inside of the chamber is approximately 1.7 cm. After approximately 180 seconds of sputtering at low pressure, nitrogen was introduced into the system, usually at a rate of 8 sccm. After 180 more seconds of sputtering, now NbN, the shutter on top of the sputtering source was opened to allow deposition of NbN onto the heated substrates and holder. Once sufficient time has passed to deposit a film of the desired thickness, the source shutter was once again closed. At this point, the heaters and gases were turned off and the cryopump gate valve was fully opened to return the system to base pressure. The substrate holder was then left in the vacuum chamber for at least five hours to cool,

often overnight, before the loading process was reversed and samples were removed from the system for testing.

Sheet Resistance:

Sheet resistance measurements were made on a Remington LLC four point probe, connected to a Keithley 2400 source meter operated in four point mode. The sourcemeter was used to source 100uA of current through the outer pins of the Remington probe, while voltage is measured across the inner pins by the Keithley. Since films were only 9 mm diameter, relatively small compared to the spacing of the four point prove pins, a geometric correction must be made to the standard formula for converting the measured resistance to sheet resistance. The diameter of the probe pins is not accounted for.

Due to the finite size of our samples we multiplied the standard sheet resistance calculation (4.53* V/I) by a correction factor (Co). This accounted for the fact that the samples are not of infinite extent:

$$R_{\blacksquare} = \frac{\pi}{\ln 2} \mathrm{C_o} \frac{\mathrm{V}}{\mathrm{I}}$$

$$\mathrm{C_o} = \left(1 + \frac{1}{\ln 2} * \ln\left[\frac{1 + 3\left(\frac{s}{d}\right)^2}{1 - 3\left(\frac{s}{d}\right)^2}\right]\right)^{-1}$$

Here *s* is the spacing of the 4 point probe pins and *d* is the diameter of the sample. For the Remington four point probe, s = 62.5 mils. Our samples have diameter of 9mm. As a result the correction factor C_o is equal to 0.7873.

Measuring the Superconducting Critical Temperature:

Measurements of resistance vs temperature were made inside of a Sumitomo Gifford McMahon cryostat capable of a base temperature of approximately 3.9K. The temperature was monitored by a Lakeshore model 34 temperature controller connected via four wires to a NIST traceable calibrated silicon diode temperature sensor with an error of +/- 12mK at 10K. The temperature sensor was screwed down firmly with a brass 4-40 screw to the OFHC copper pieces which make up the sample holder. The sample holder was constructed from multiple ¼ inch thick OFHC copper sheets which were cut in a water jet cutter and assembled using brass 4-40 screws. Two small copper blocks were the only thermal connections between the cold head and the sample holder, providing thermal resistance between the coldhead and the samples. This was done in order to thermally low-pass-filter the sample holder, reducing the amplitude of temperature variation at the sample stage relative to the cold head. Six 1cm by 1cm samples could be loaded onto the sample holder at once, and connected to the outside of the cryostat via twisted pairs of 36 AWG phosphor bronze wire. Each of the four wire connections was wound tightly around a heat sink bobbin that was attached to the base of the sample holder. Apiezon grease was applied to the heat sink bobbin / wire assembly to improve thermalization of the wire. These 24 wires were connected to a 32 pin vacuum feed through along with the four wires connected to the temperature sensor, and two wires used to power the heater attached to the bottom of the sample holder. Six samples could be loaded into the sample holder at one time. After closing the 40K radiation shield, the outer vacuum jacket can be installed and the system pumped down to ~8e-5 torr before being cooled down to base temperature.

Resistance of the samples was measured in the following way. A 10 microampere constant current source, along with two 16 bit analog to digital converters were multiplexed to one sample at a time. The multiplexers used were Analog Devices part number ADG707BRUZ which have low on state resistance of 2.5 ohms and a very low leakage current of 100pA. A labjack data acquisition board connects to a PC via USB and provided both the ADCs as well as the control logic that drives the multiplexors. Measurements of resistance vs temperature for the six samples was fully automated. After loading the samples and initiating the custom Python software, the cryostat was turned on. The resistance of each of the samples was recorded at 5 second intervals from room temperature down to ~4K. Once the cryostat reached a designated temperature, the multiplexor was set to one channel (switching between all channels ceases) and the resistance was recorded continuously at a sampling rate of approximately 5Hz while the temperature of the coldhead was ramped up to >20K, typically over the course of 10-60 minutes. Resistance was also monitored as the heater was slowly turned off and the temperature returned to the base temperature. Measurements while ramping the temperature up and down were checked for hysteresis to ensure the accuracy of the T_c measurement. The superconducting critical temperature was taken by convention to be the temperature at which the sheet resistance was 50% of its value at 20K. This value, along with the 90%-10% resistance width, known as delta-Tc, and the residual resistance, which is the resistance at room temperature divided by the resistance at 20 K, was recorded. The compressor was then turned off and the heater turned on to return the sample holder to room temperature. A small amount of helium gas was usually added to the chamber to increase heat exchange between the cold parts of the system and the 293K outer vacuum chamber.

Transmissometry:

The thickness of few-nanometer-thick metallic films is necessary information for calculating the film resistivity and for analyzing the behavior of devices fabricated from this film. A home built optical transmissometer was used to estimate the thickness of NbN films on MgO substrates. By measuring the amount of light transmitted at normal incidence through the film and substrate, the thickness of the film can be estimated by fitting to an optical model using known optical constants. The matrix transfer method is used to estimate the thickness based on the experimentally observed transmission, taking into account sufficient internal reflections in the film such that additional rays do not change the derived thickness.

X-ray Reflectivity:

Our home built optical transmissometer relies on assumed optical constants, which are known to vary based on how NbN films are deposited, so thickness measurements based on x-ray reflectivity were used to confirm the thicknesses estimated with the transmissometer. X-ray reflectivity measurements were made using a Rigaku SmartLab in a shared facility. Copper Ku alpha x-rays were generated with a 9kW rotating anode x-ray source and directed towards the surface of the NbN thin films. By varying the angle of the incident beam and recording the intensity of the reflected beam at the same angle, an interference pattern can be observed due to the reflection from the NbN /air interface interfering with the reflection from the NbN/substrate interface. The resulting interference pattern can be fit to a model using known indices of refraction in order to determine the thickness and density of the NbN film. The software GlobalFit was used to create a model to fit the recorded data.

Rapid Thermal Processing:

Rapid thermal processing can be used to increase the Tc of NbN films. A rapid thermal processor was used to heat NbN films from room temperature to 1000C in less than 60 seconds. The temperature is monitored by a pyrometer inside of the chamber. The samples were loaded onto a silicon wafer and the chamber closed. Argon or nitrogen was then flowed into the chamber. The samples were then heated to ~1000C, held at this temperature for three minutes and then cooled back to room temperature as quickly as the system would permit. The chamber temperature would drop quickly initially, but would require about 15 minutes to reach 20C.

Chapter 5

Experimental Results and Discussion:

In order to engineer superconducting devices based on reactive DC-magnetron-sputtered ultrathin-film niobium nitride (NbN), we require the ability to deposit high-quality material with properties that are predictable over time. The quality of the material is judged primarily through its superconducting critical temperature (T_c) at a desired thickness. The T_c of thin films of NbN is affected by variables that include: film thickness [1], chemical composition [2], crystal structure, and defect concentration [3]. These variables are strongly influenced by the deposition conditions. However, due to the complex interplay between the system inputs and the resulting film, the conditions which optimize the T_c of thin film NbN must be determined empirically. This chapter summarizes the results of our efforts to increase and control the T_c of ultra-thin NbN films by controlling the system deposition parameters as well as methods used to increase T_c beyond the system's optimum.

While a substantial number of these films were deposited on crystalline MgO and Al2O3, our initial experiments on MgO proved to have poor reproducibility. This, combined with success fabricating SNSPDs on silicon based substrates, led us to focus our efforts on NbN deposited on amorphous silicon nitride and silicon dioxide on silicon. Therefore, the results

presented here refer almost exclusively to NbN on SiN_x and SiO_2, with the biggest exception being optical thickness measurements made on NbN films deposited on MgO.

Reproducibility: Short-Term, Among Substrates, and Long-Term:

In order to draw conclusions from experiments meant to improve the T_c of NbN thin films, we must first characterize the short and long-term variability of the properties of the films deposited under nominally identical conditions. Short term refers to depositions done within days of one another, typically in sequence with no other processing done in the chamber between depositions, while long term refers to everything else from weeks to months or longer.

Figure 5.1 shows the results of resistance versus temperature measurements of six NbN films deposited in three identical depositions onto thermally oxidized Si substrates. These depositions took place over the course of three days and were the only processes undertaken during that time. The T_c of the film is taken by convention to be the temperature where the sheet resistance has fallen to 50% of its value at 20K (see methods). The mean T_c for these films was 11.57K with a standard deviation of 51.6mK. These values allow us to quantify the likelihood that an observed T_c value of an NbN film is due to uncontrolled variation in the system or whether it is due to our experimentation. For most of the results that will be illustrated, a series of films were deposited for the purposes of fabrication before an experiment was performed. Films deposited for fabrication thus had a dual role: the raw material for device fabrication as well as the control samples to compare with experimental ones. T_c measurements from experiments will be contrasted with a short term baseline in order to judge the effect of the experiment.

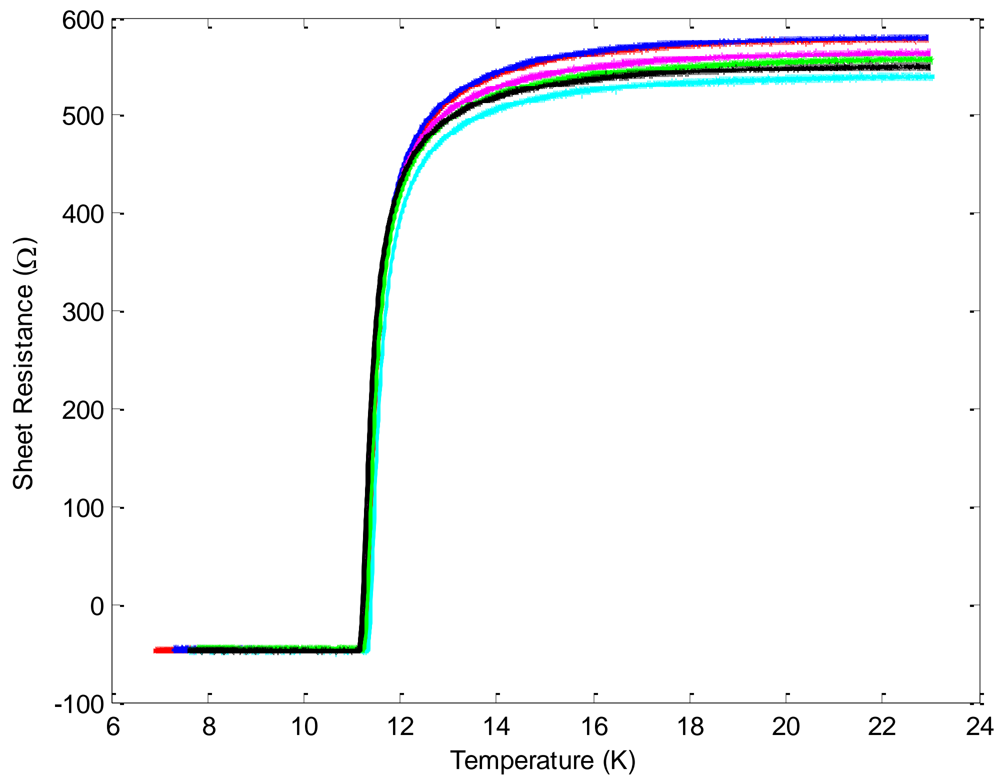

Figure 5.1: Resistance vs temperature measurements of six ultrathin NbN films deposited on thermally oxidized Si. Films (SPE078, 079, 081, 082, 084, 085) were deposited in three sequential runs (391, 392 and 393) of two films each, with identical deposition parameters over the course of three days. Each deposition also included an MgO substrate which was used for optical thickness estimates.

T_c of NbN on SiN_x and SiO_2:

In order to facilitate fabrication of different types of devices, some of our experiments with NbN were performed on thermally oxidized Si substrates, while others were performed on

chemical vapor deposited SiN_x. SiN_x and SiO_2 both have amorphous structure, however it is not obvious beforehand that NbN deposited on these two substrates will be the same. For instance, differences in interfacial mixing, chemistry and intrinsic strain of the SiN_x or SiO_2 layer could lead to differences in the resulting NbN. Differences in material properties due to substrate differences could influence the design of subsequent devices. We therefore investigated whether NbN films grown on these two substrates have the same T_c. As it turned out, answering this question also made it easier to determine how consistent the system is over long periods of time since the substrate was often dictated by the needs of fabrication and thus long periods of growing on one substrate or another were common.

Figure 5.2 shows that NbN films deposited on SiN_x and SiO_2 have identical transition temperatures when deposited separately with the same deposition parameters. These two depositions were done approximately eight days apart with two intervening depositions. Each deposition included one MgO substrate that was used for optical thickness measurements. These thickness measurements were 4.5nm and 4.56nm for the SiO_2 and SiN_x deposition respectively. The room temperature resistance measured with a standard four point probe of these two batches of films was slightly different, the mean (standard deviation) being 430(3.4) ohms and 465(0.9) ohms for the films on SiO_2 and SiN_x respectively. The SiN_x layer was measured by ellipsometry to be 336nm while the SiO_2 was measured to be 229nm. These thicknesses were in use prior to switching to 172 nm and 255 nm. Both substrate types were prepared with the same cleaning process (see methods).

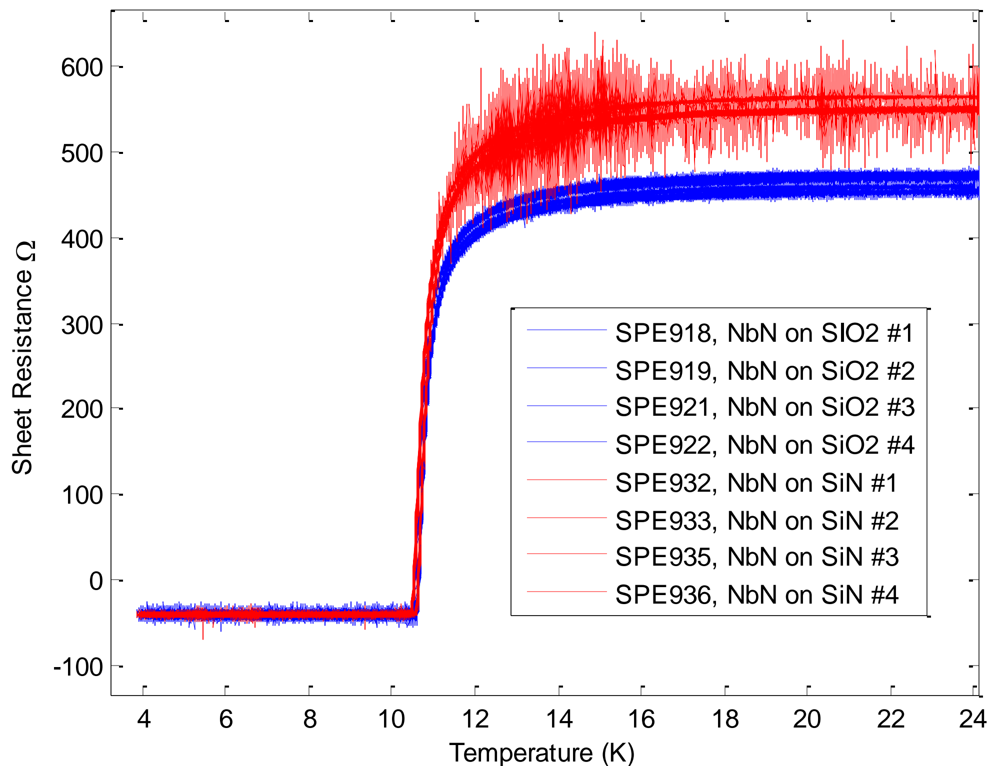

Figure 5.2: Resistance vs temperature measurements of NbN on SiO_2 (blue, run # 345) and SiN_x (red, run # 348). The mean T_c of the films on SiO_2 was 10.83K with a standard deviation of 49.9mK. For the films on SiN_x the mean T_c was also 10.83K with a standard deviation of 48.6mK. An unidentified additional source of electrical noise was present for the T_c measurement of the films on SiN_x that was not present during other measurements of the T_c on either substarte.

Long-Term Reproducibility:

Figure 5.3 illustrates the difficulty with comparing identical depositions done more than a few weeks apart. Resistance versus temperature measurements from figure 5.1 are reproduced in red, while measurements from six films created in identical depositions done in sequence

(depositions 416, 417 and 418) six weeks later are shown in blue. Not only has target erosion caused the deposition voltage to drop by ~9%, but a noticeable wobble of the substrate holder developed in the interim, which we believe caused the additional spread and bimodality in both Rs and T_c. This issue with the substrate holder wobble developed at the end of this work. Most of the discussed data was taken prior to this development.

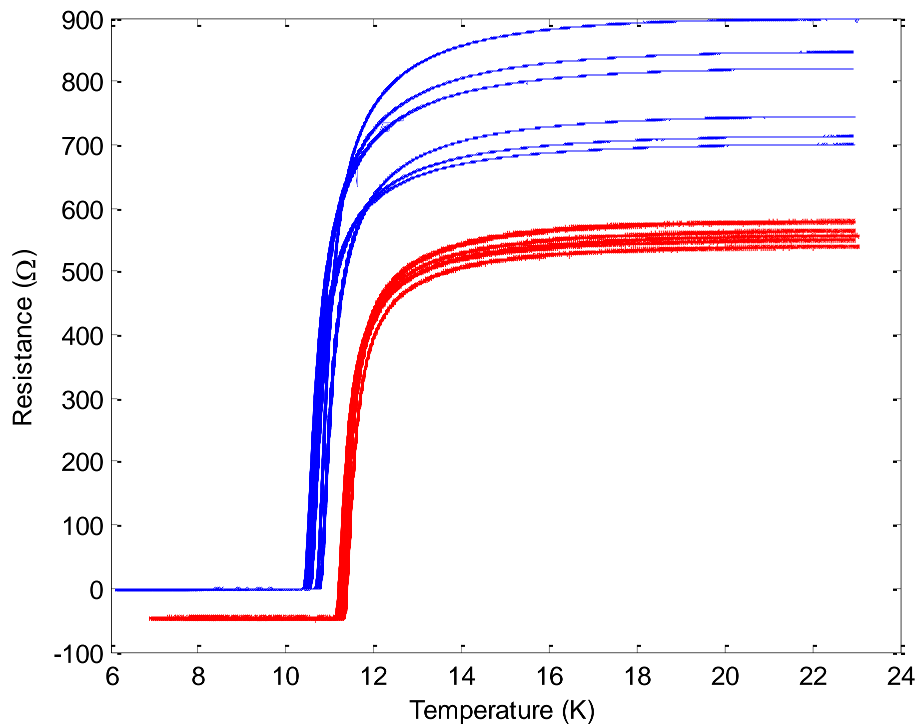

Figure 5.3: Long-term stability of T_c on SiO_2 substrates. Curves in red are reproduced from figure 1. Curves in blue are from three sequential depositions onto two SiO_2 substrates each, with identical depositions parameters to those shown in red. The resistance offset of the red curves was reduced by improving the signal chain used to measure voltage across the films (see methods).

Long-term reproducibility as judged by the thickness measured with the transmissometer (see methods) seems more consistent than T_c measured on films on Si based substrates. In most depositions, an MgO substrate was included to collect NbN for use with the optical

transmissometer. These films are referred to as 'sisters' to the films that were used for fabrication. Figure 5.4 shows the thickness of sister MgO chips measured over the course of a month, along with the T_c of SiN_x and SiO_2 films deposited at the same time. For identical deposition parameters, the thickness of the resulting films were the same to within 1.7 Angstroms or about 4.7% of the mean thickness of the films measured. Tc for the SiNx and SiO2 sister films varied by 8.7%. The dashed line in figure 5.4 indicates when the Nb deposition target was changed. This change resulted in the deposition voltage rising by about 13.2% (as judged by the pre-deposition spark power). We have reason to believe that the change in deposition voltage as a result of target erosion can change the T_c of the deposited film by changing the energy of reflected neutral atoms that bombard the growing film and affect the film microstructure, which may be the cause of the 300mK rise in the mean Tc after changing the target. Also, it is possible that the deposition rate is higher when the target is eroded, because the angle at which the impinging argon ions meet the target is effectively reduced below 90 degrees. As noted in chapter 3, for the same ion energy, sputtering yields are higher for smaller angles.

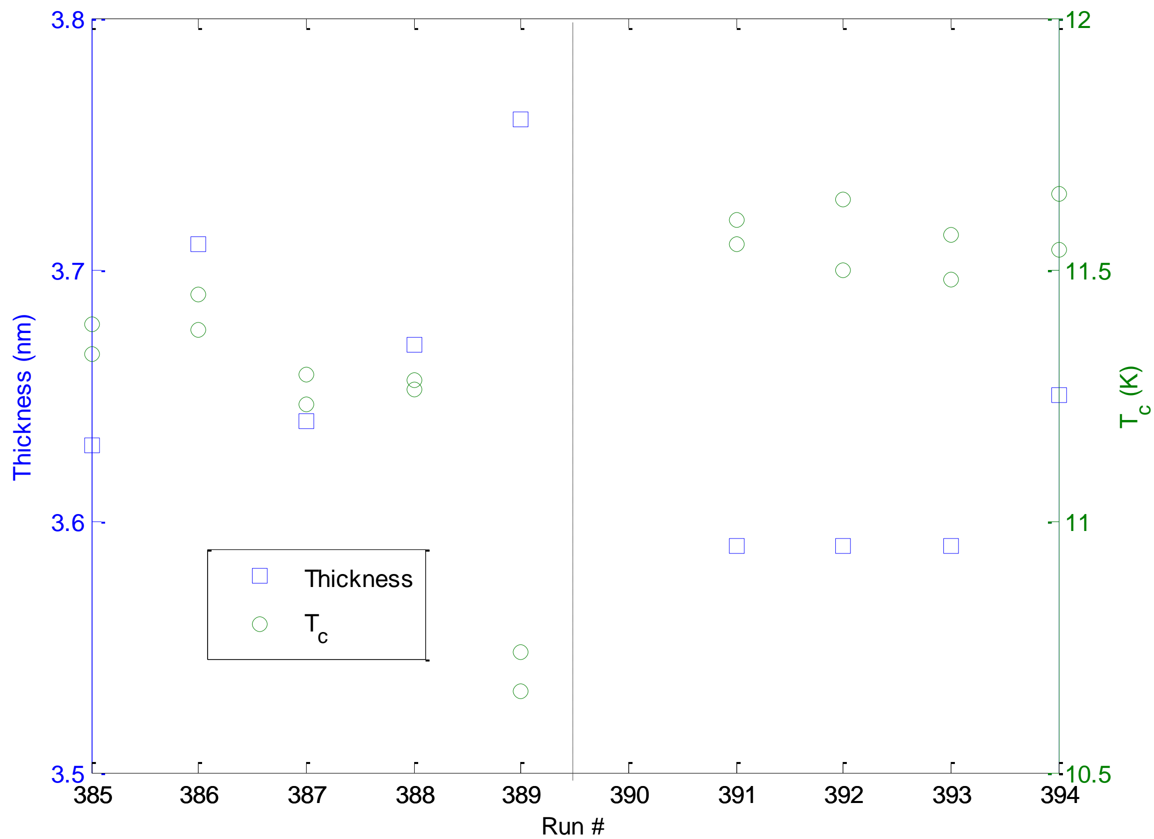

Figure 5.4: Thickness of NbN films on MgO deposited at the same time as films on SiN_x and SiO_2 with T_c of SiN_x and SiO_2 films. All of the displayed runs were nominally identical. After run 389 the niobium target was changed causing the deposition power to rise by 13.2% in run 391. The mean T_c of NbN on SiN_x deposited in runs 386-388 was 11.3K with a standard deviation of 83mK, while the mean T_c of NbN on SiO_2 deposited in runs 390-394 was 11.6K with a standard deviation of 61mK.

The above results set the stage for us to experiment with the deposition process in order to improve the T_c of thin NbN films and understand what sputtering conditions yield films with desired properties. The improved degree of reproducibility that the T_c of NbN films on SiO_2 and

SiN_x exhibit over short time scales allows us to make conclusions that were previously impossible to make when depositing films on MgO.

Design of Experiments:

Prior to this work, our group did not regularly heat silicon-based substrates in our deposition system due to the potential for violent reactions that can occur between the nickel in the substrate holder and silicon at elevated temperatures [4]. We observed this reaction when trying to deposit at 800 °C on a bare silicon wafer; the wafer shattered and the substrate holder became covered in reaction products. In order to avoid this, we coated all surfaces that could potentially come into contact with the substrates with 100s of nanometers of NbN. This coating allowed us to safely heat silicon-containing substrates to high temperatures without the risk of compromising our deposition chamber.

Prior to this work, we only deposited on SiN_x at room temperature. Heating to 800 °C was a substantial change to how we deposit on SiN_x, we therefore conducted a brief design of experiments to try to determine the optimal deposition parameters for NbN grown on SiN_x heated to 800 °C. We decided on a few parameters to vary while keeping all other process variables constant. The variables that we decided on were the nitrogen flow rate and the total pressure during the deposition. The parameters held constant were: the temperature, which was fixed at 800C for all depositions, the Argon flow rate, which was kept at 26.5 SCCM, and the deposition time, which was held at 90 seconds. The variables and results are summarized in Table 5.1.

Sample	Run #	N2 Flow Rate (sccm)	Chamber Pressure (mTorr)	Measured Deposition Voltage (V)	Thickness (nm)*	R_sheet (Ω)	Tc (K)	ΔTc (K)	RRR
SPD655	265	6	3.5	455	5.3	299	11.0	1.07	0.72
SPD660	266	8	2.5	458	5.1	352	11.3	1.19	0.73
SPD665	267	8	4.5	463	4.2	539	9.4	1.62	0.67
SPD666	268	4	4.5	440	7.1	389	6.7	0.72	0.83
SPD671	269	4	2.5	440	10.5	301	4**	----	0.99

* Average thickness of three NbN on MgO sister chips in same run
** Estimated from R vs T curve that was beginning to transition when lower temperature limit was reached

Table 5.1 Design of Experiments on SiN_x. The substrate temperature was held constant at 800C for all runs. The Argon flow rate was constant at 26.5 SCCM and the deposition time was always 90 seconds.

Qualitatively, the results of the DOE are consistent with a simple interpretation of how we can maximize the T_c at a given thickness: by depositing a film that is as close to being mono-crystalline as possible with the right ratio of niobium to nitrogen. Depositing such a film can be understood in terms of the revised structure zone model (RSZM) of thin film growth [5]. While the original zone growth model of Thornton [6] predicts that film structure will largely be determined by the reduced temperature (which is the substrate temperature divided by the melting point of the deposited material) and pressure, the RSZM includes the effect of bombarding the substrate with energetic particles as they will deposit energy into the growing film, increasing the mobility of deposited species and reducing the likelihood of voids and other non-idealities. While the effect of bombardment energy was probed by directly applying a DC bias to the substrate holder during sputter deposition in ref, other workers have concluded that the voltage used during sputter deposition will determine the distribution of energies of both sputtered material and reflected neutral gases that will bombard the surface of the growing film

[7]. Therefore, the accelerating voltage used during the deposition is almost as important as the temperature during the deposition.

While the target voltage is important due to the bombardment energy that it can add to the nascent film, we typically do not operate in a voltage mode during the deposition. This is because voltage biasing during reactive sputtering is not stable for partially reacted targets—in voltage mode, the only stable states are a target surface that is fully unreacted or fully 'poisoned' or covered by the compound. This prevents us from tuning the film stoichiometry. See Sputtering theory section for more.

One other fact necessary to understand the results from table 5.1 is the effect of the chamber pressure. It can be understood as a mechanism for both sputtered material and reflected neutrals to lose energy on route to the substrate by scattering off of gas molecules. Higher chamber pressure means less bombardment energy to promote diffusion on the surface of the film. On the other hand, higher pressures mean a more conductive plasma and a greater amount of material sputtered form the target.

Finally we can see that the film with the highest Tc form the design of experiments, SPD660, (though not necessarily optimal) resulted from a low chamber pressure and a high nitrogen flow rate. The nitrogen flow rate helps determine the sputtering voltage, which in turn affects the bombardment energy. As seen in Figure 5.5, the target voltage is a monotonic function of nitrogen flow rate. Though SPE665 was deposited with the same nitrogen flow rate, the high chamber pressure results in lower bombardment energy and may also be responsible for the reduced thickness of the film, as the higher chamber pressure may have caused the sputtered material to assume more diffusive movement towards the substrate, expanding the solid angle of the material flux and thus dropping SPE665's thickness.

Comparing film thicknesses derived from our optical measurement transmissometer should be done with caution as it is unclear how different the optical constants of films grown under different conditions will be and there is evidence that film reflectivity may vary by three times for films deposited at different pressures [8]. For example, n and k will vary as the nitrogen flow rate is changed. In ref [9] NbN was deposited at different nitrogen flow rates and the optical constants were measured by ellipsometry. This ellipsometriuc data can be converted into n and k. By varying the nitrogen flow rate of NbN_x films deposited at room temperature, n varied between 1.8 and 3.1 while k varied between 2.3 and 3.2. If the optical properties of our films vary in a similar way, this could induce an error in the transmissometer measurement of the thickness of up to 25%, enough to make it difficult to distinguish T_c differences due to chemistry and those due to size effects.

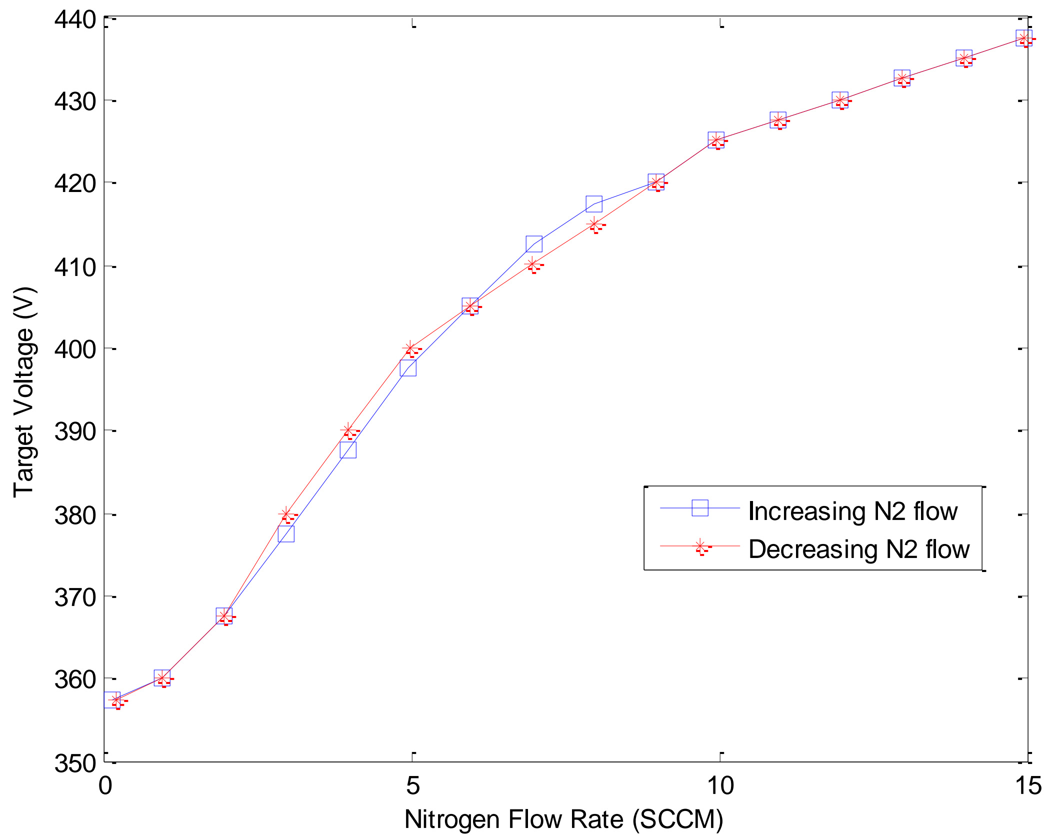

Figure 5.5: Target voltage vs nitrogen flow rate. This data was collected in a current-controlled mode with i=400mA with the shutter of the sputter gun open. The Argon flow rate was fixed at 26.5sccm and the chamber pressure was maintained at 2.5mtorr. Nitrogen was introduced into the system in steps of 1sccm per step. At each step, the flow rate was maintained for 2 minutes to account for any thermal effects that could arise due to increased power dissipation at the gun. No hysteresis was observed upon reducing the nitrogen flow rate back to zero.

Due to the difficulty in disentangling the thickness contribution to the measured T_c from the microstructure and stoichiometry, other workers depositing NbN thin films have simply varied the nitrogen flow rate while keeping all else fixed. However, this is often incorrectly interpreted as finding the optimal film stoichiometry. In reality, doing such measurements allows

one to find the optimal balance between film stoichiometry and microstructure, as the reactive gas will change the target voltage, changing the bombardment energy and thus the film microstructure.

While further optimization is likely possible, films deposited with the same conditions as SPD660 showed promising results when fabricated into detectors, and, as a result, we keep these deposition settings while performing further experiments.

Improving the Substrate Holder:

The original substrate holder was comprised of three Inconel parts screwed together: a 4" diameter, 0.25" thick circular base that could interface with the deposition system such that the entire substrate holder could be held suspended upside down above the sputter guns in the center of the vacuum system; a plate, also 4" diameter circular piece, ~0.2" thick which contains pockets into which 1cm by 1cm substrates could be placed and can be screwed into the base; and finally, a face plate that would serve the dual role of preventing the substrates from falling out of the assembly during loading and deposition as well as acting as a shadow mask in order to deposit circular films with a 9mm diameter.

We noticed during depositions that the plate and face plate that the substrates were sandwiched between would remain dark and grey in appearance, even when the base was glowing red and the system thermocouple was reading 800 °C. This coloring indicated that the samples were not getting as hot as possible which is important in the zone structure model of film growth.

In order to remedy this failure to heat, the base was machined to include six pockets just large enough to fit 10mm by 10mm by 0.5mm samples into. In addition, large holes (~1cm diameter) were drilled into two of these pockets to provide a line of sight path between the heat lamps and the substrates loaded into these pockets. We refer to these as the 'open' slots in the substrate holder, while the other four are 'closed'. Typical T_c measurements from open and closed slots are compared in Figure 5.6 in blue. Films grown in the open slots have substantially higher T_c and lower resistance than their closed slot counterparts despite being deposited at the same time. In Figure 5.6, the closed-slot film SPE024 has a T_c of 10.7K and room temperature sheet resistance of 505.6 Ohms/square, while the open-slot film SPE025 has a T_c of 11.8K and a sheet resistance of 412.1 Ohms/square.

Backside Absorber:

The improved T_c of films deposited in open slots is likely a result of increased substrate temperature due to being heated directly from the heat lamps, instead of being heated by the Inconel substrate holder which is heated by the lamps. Of the possible heating mechanisms, convection, conduction or radiation, only radiative heating is substantially changed from a closed slot to an open slot, with the same deposition parameters. It may be possible to increase substrate temperature during deposition by enhancing the absorption of radiant heat with a layer of NbN deposited on the back of the substrate.

Conductive and convective heating are not likely to have influenced the difference in T_c between films deposited in the open and closed slots. All of the substrates are held loosely by the holder, such that the only mating force between the substrate and the Inconel is the weight of the

substrate. Thus, the thermal boundary conductance between the Inconel holder and the substrate is likely vanishingly small, and as a result, the conductive heating should be negligible. Further, the faceplate/substrate/holder, when installed into the deposition system, is oriented such that the substrate is being suspended by the faceplate and out of contact with the other Inconel surfaces. The faceplate is the same for each of the slots, except for very small notches cut into each opening, so that the shadowing creates identifying marks in the resulting films. Thus, any conductive heating should be the same in both open and closed slots. Convective heating should be close to the same as long as the gas pressure is kept the same. However, having less 800C Inconel in close proximity may mean less heating in the open slot due to convection.

We attempted to further increase the effectiveness by which substrates were radiantly heated by depositing a small amount of NbN onto the backside of SiN_x substrates to act as a heat absorber. The thickness of this absorbing layer was chosen to be 9nm, slightly thicker than the optimal thickness for absorbing 1550nm light for unpatterned NbN on SiO_2 without an optical cavity [10]. The effect on T_c of adding this backside absorber layer is shown in red in Figure 5.6 in order to compare with the no absorber case for both open and closed slots. SiN_x substrates with a 9nm layer of NbN on the backside of the films showed a decrease in T_c by 600mK for the film in the closed slot and about 300mK for the film in the open slot. In addition their sheet resistances were slightly reduced.

It is unclear why the backside absorber would reduce the T_c of the film; however, it may simply be that at the substrate temperature that results from the absorber, the T_c must be re-optimized with respect to the nitrogen gas flow rate, as is often done for different operating pressures [2]. This is consistent with a shift in chemistry due to improved heating, the films with

the backside absorber had a lower sheet resistance and a lower Tc, which could be expected if the NbN_x film is nitrogen deficient.

Lastly, while the addition of a backside absorber onto SiO2 substrates may require optimization of the nitrogen flow rates in order to show improvement in the maximum T_c possible, results on MgO were less ambiguous. By adding an absorber onto an MgO substrate, we were able to achieve a T_c higher than 16K with a film approximately 30nm thick. Previous films of similar thickness had lower T_c.

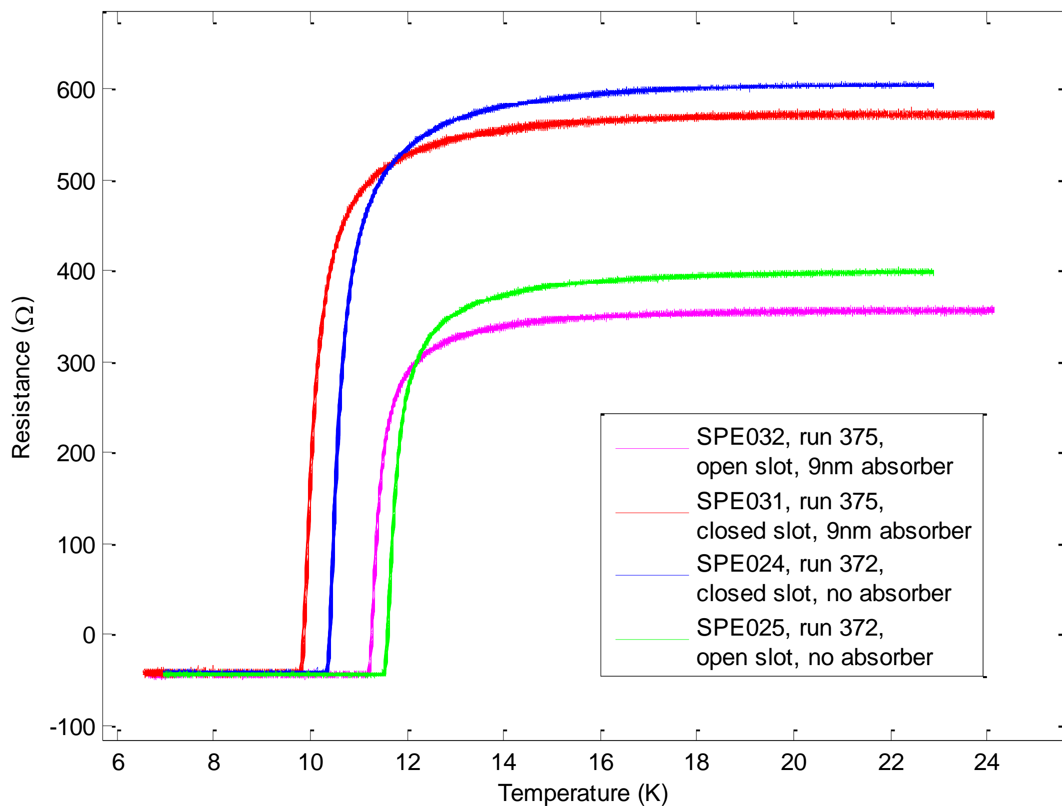

Figure 5.6: Open (magenta and green) and closed (red and blue) slots, with (red and magenta) and without (blue and green) ~9nm backside absorber. Resistance curves for films from the open slots always exhibit higher T_c (11.5K and 11.8K vs 10.7K and 10.1K) and lower sheet resistance (390

and 412 Ohms vs 487 and 586 Ohms) than films deposited at the same time in closed slots. Here, films from run 372 are shown in blue and green. Films from run 375 had approximately 9nm of room temperature NbN deposited on their backsides before being deposited in an identical manner to the films shown in comparison, including slot number.

Bias Sputtering:

Our deposition equipment allows us to apply an RF bias to the substrate holder which can be used to spark a plasma and sputter from the substrates. This process can be used to sputter clean the samples prior to deposition as well as allowing us a means of adding ion bombardment to the growing film during deposition. Based on the RSZM, it would seem that the application of this bombardment would improve crystal microstructure. This result appears to be the case for films in the closed slots of the substrate holder, as the addition of 40W of RF power increased the T_c of films in the closed slots. However, for films in the open slots, the opposite was observed. These results are shown in Figure 5.7.

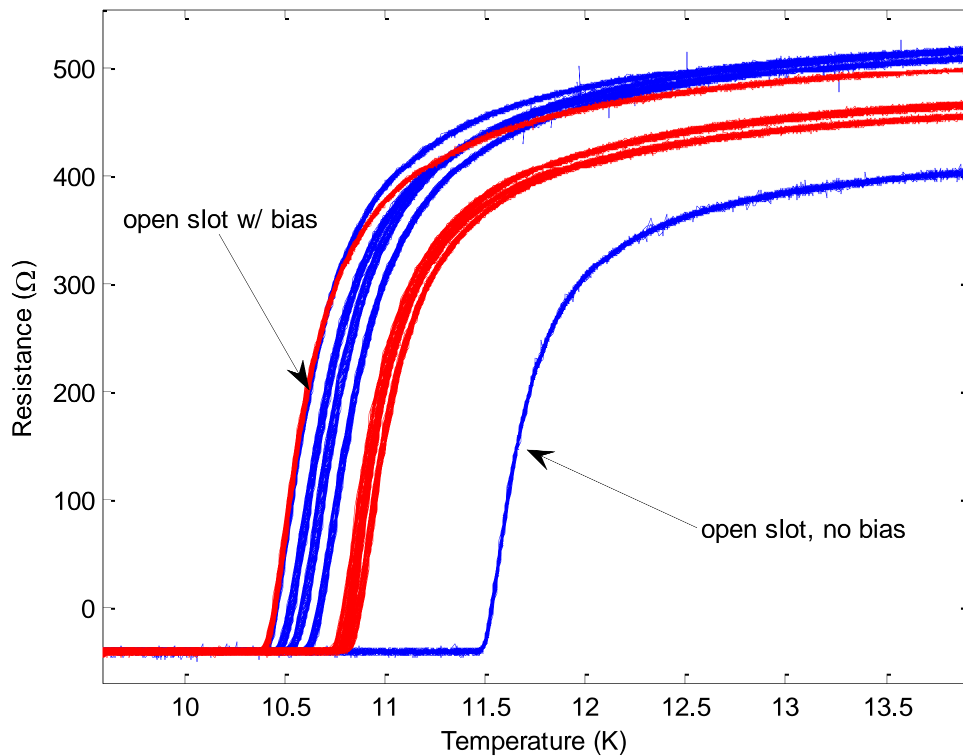

Figure 5.7: 40W RF Bias Sputtering experiment. Films (all on SiO_2) from run 357 had no bias sputtering and are shown in blue, while films from run 358 had a 40W RF bias applied during the entire deposition process, both depositions were otherwise identical. Notice for both blue and red curves there is a central grouping with one curve that is split off from the rest. In both cases this split-off curve is the film grown in the open slot. The T_c of the open-slot film without bias was 11.7K, however when the bias was applied in the next run, the open slot T_c fell to 10.7K, below the average T_c of the films from closed slots. The bias improved the mean T_c of the closed slots from 10.8K with a standard deviation of 101mK to a mean of 11.1K with a standard deviation of 25mK. Reflectometer measurements of thickness on a sister MgO film were 4.14nm and 4.34nm for runs 357 and 358 respectively.

It is possible that the reduction in T_c in both the case of the added backside absorber as well as the open slot film with bias are related to increased effective heating and that some shift in the ideal amount of nitrogen contained in the film is necessary to realize a global increase in T_c. Determining the change in the maximum T_c would require repeating the design of experiments with only the nitrogen flow rate as a variable with bias sputtering and/or backside absorbers added as constants across the experiment. However, since this is a lengthy process and uncertain to yield improved T_c, this avenue was not explored.

Rapid Thermal Processing:

Without large scale infrastructure upgrades, the T_c of films deposited in our system seem to be as high as we could expect and comparable to the highest T_c s recorded for 4-5nm thick NbN [11]. However, it is natural to wonder whether we can easily increase the T_c of our films beyond the system limits in some *ex situ* process. Rapid thermal processing (RTP) was previously explored as a means to increase the T_c of 20nm NbN and NbTiN on Al2O3 [12], but attempts on SiN_x substrates were not successful [13]. Rapid thermal processing is a technique used commonly in semiconductor manufacturing to heal minor structural damage due to ion implantation. We explored using RTP to improve the T_c of 4-5nm films of NbN deposited on SiN_x.

We used the RTP to heat films to ~1000C in a matter of seconds in various gaseous environments for varying lengths of time. The hold time at high temperature, the gaseous environment, and the speed with which the samples were heated and cooled was varied. In general, most films had their T_c increased to close to 13K regardless of starting point. This

translates into a 1K increase for our highest T_c films, and 2-3K increase for suboptimal films; even greater increases are seen for films deposited at room temperature (see below). Resistance vs temperature measurements before and after RTP is illustrated in Fig 5.8.

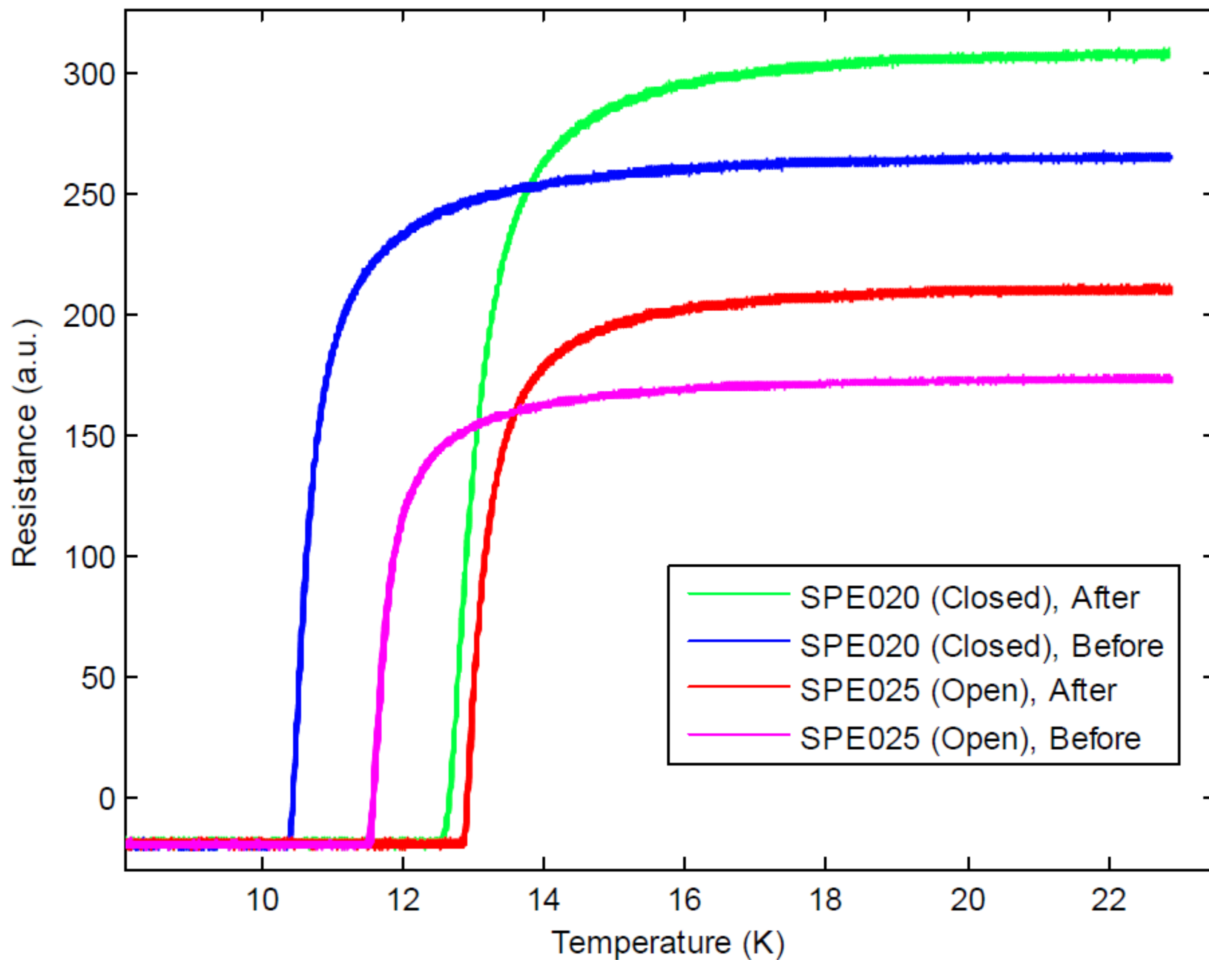

Figure 5.8 RTPing NbN on SiN_x to improve T_c. Films SPE020 and 025 were deposited together initially but from closed and open slots respectively. Both were then RTPed using the same recipe: while flowing 10SLPM of N2, ramp temperature from room temp to 1000C in 90s, hold at 1000C for 3 minutes and then ramp back to room temperature in 45 seconds. The T_c of both films increased dramatically; the T_c of SPE020 increased by 2.3K to 13.1, and SPE025 increased by 1.4K to 13.2. Both films showed marked increases in sheet resistance, though this was later

shown not to be reproducible (note: the y-axis here must be multiplied by 2.3 in order to get real Rs).

We used Argon in place of Nitrogen during RTPing in order to determine whether the RTPing process was increasing film T_c by shifting the Nb/N ratio. We found a similar increase of T_c to close to 13K using both gases. This is shown in Figure 5.9. One thing to note here is that the same experiment was repeated later, using our now standard RTP recipe with Argon and then Nitrogen gas on films that were grown together and started off almost identical. The dramatic increase in Rs that is shown in Figure 5.9 was not observed later; rather, a reduction of Rs by 24% was later seen while RTPing in Argon. It appears that while the RTP may reproducibly increase T_c to ~13K, the change in Rs is dependent on the preceding use of the machine. When the RTP was only used for these experiments the eventual result after multiple runs was that the film Rs would drop in addition to increasing T_c as one would expect from studies of superconductor Tc as a function of dislocations from exposure to high energy neutrons. However the jump in film Rs in addition to increased film T_c provides an interesting test case for any theory regarding the superconductor to insulator transition.

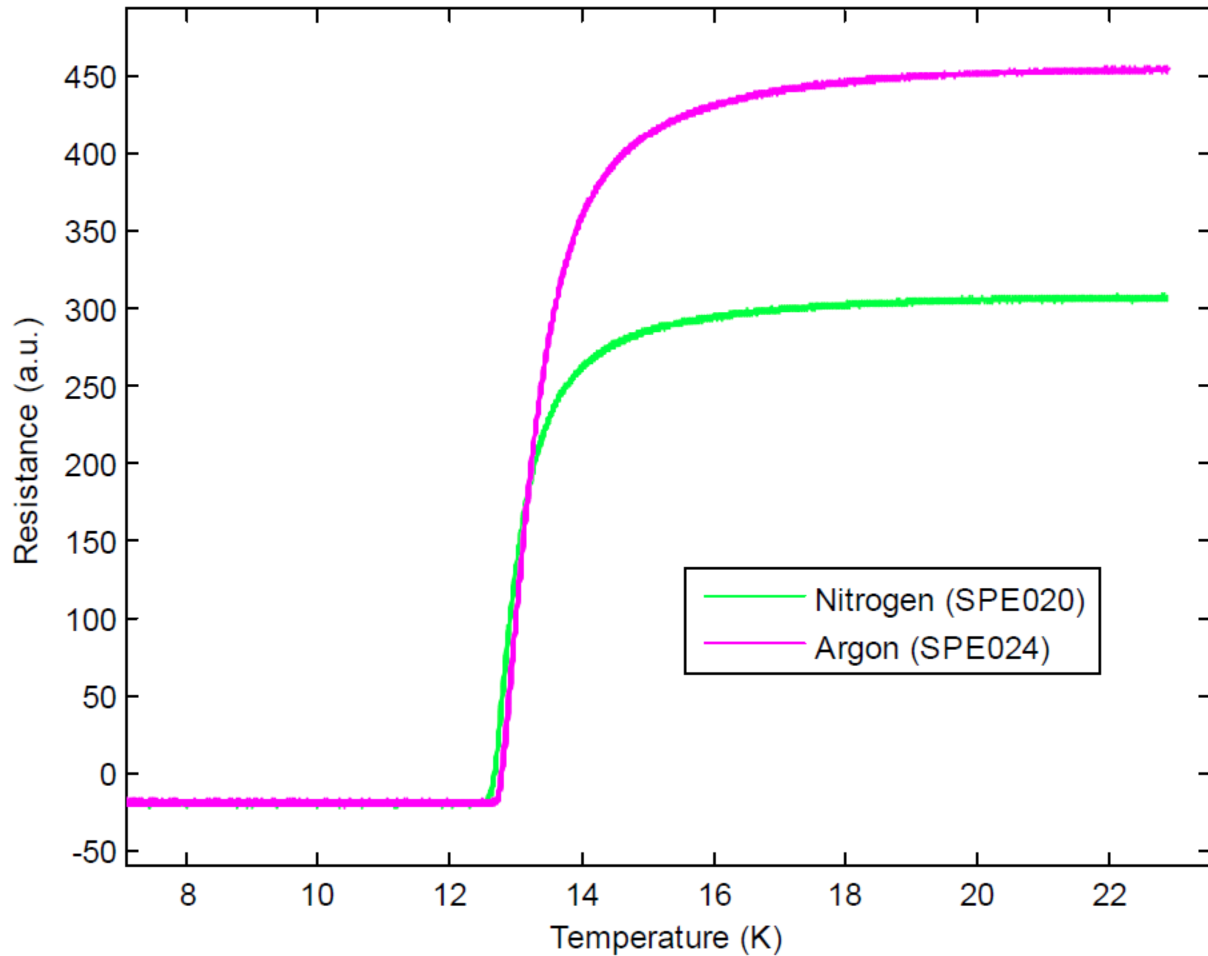

Figure 5.9: Process Gas effect on RTP results. SPE020 and 024 were deposited together and measured to have near identical properties. After RTPing with our standard recipe in Argon and nitrogen, both exhibited T_c slightly higher than 13K. The large increase in Rs observed in both films was not repeatable and appears to be linked to prior use of the RTP tool. After several uninterrupted uses of the RTP, samples continued to improve in T_c to close to 13K while sheet resistance increase slowly lowered and finally became negative (decreased sheet resistance). These results show that the RTP was not affecting the film chemistry by adding nitrogen to the film.

We attempted to determine the origin of the T_c increase by taking AFM measurements of the surface roughness, as well as material analysis by Auger electron and x-ray photoelectron spectroscopy. AFM measurements of RTPed film SPD908 shown in Figure 5.10 yielded the same surface roughness over a 10 micrometer squared area as a film that had not been RTPed.

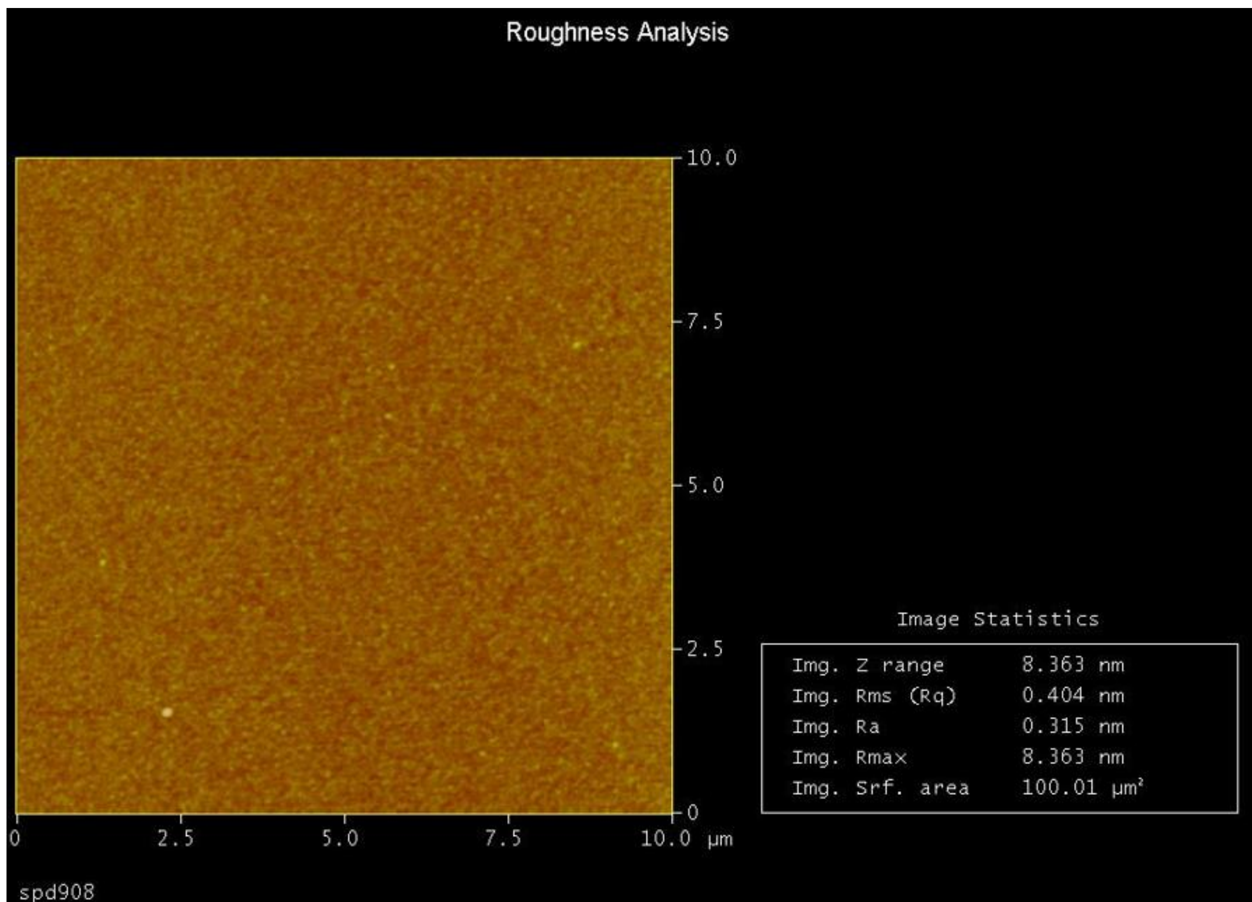

Figure 5.10: roughness analysis of SPD908 after RTPing. The RMS surface roughness of SPD908 was essentially identical to a film that was AFMed as grown. This indicates that the increase in T_c is not due to large scale conglomeration of NbN material on the surface, though other workers did notice a slight reduction in surface roughness by AFM from 0.13nm to 0.109nm.[14]. Our results are likely limited to the achievable resolution of AFM used.

Auger and XPS measurements made on RTPed films show the presence of Silicon on the film surface that is not seen on films that have not been RTPed. However, it is unclear whether this silicon diffuses up from the SiN_x substrate or whether it comes from the silicon wafer used to hold the samples during RTP. Auger measurements of an RTPed and as grown film are shown in figure 5.11.

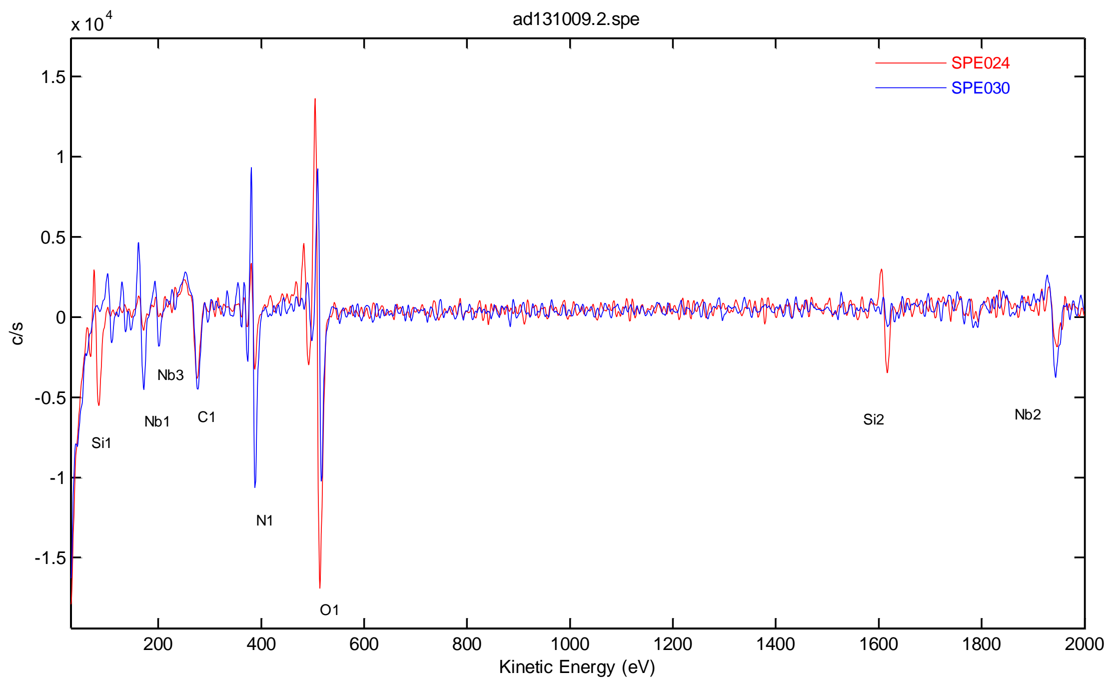

Figure 5.11: Auger electron spectroscopy for SPE024 and SPE030. These films are nominally identical except that SPE024 was RTPed using our standard process. Counts are observed for SPE024 near 80keV and 1600 keV that have been matched to silicon. The peaks are much less prominent or non-extant in the film that was not RTPed. It is still unclear if the mechanism of increased T_c is directly related to the presence of Si, or if it just happens to be coincident with another T_c increasing mechanism such as strain relief, reduction of dislocation, and general improvement of crystalline quality.

X-ray Reflectivity:

The odd results of these RTP experiments further increase our need to find a non-destructive way to measure the thickness of the deposited films when other more common means fail. One method that we investigated is x-ray reflectivity (XRR) measurements, which rely on the interference of reflected x-ray beams from the top and bottom surface of epitaxial films in order to measure film thickness. In Figure 5.12, we see the counts versus angle of the incident x-ray beam for our RTPed film in 5.12(a). Results of XRR measurements on a film on MgO is shown for comparison.

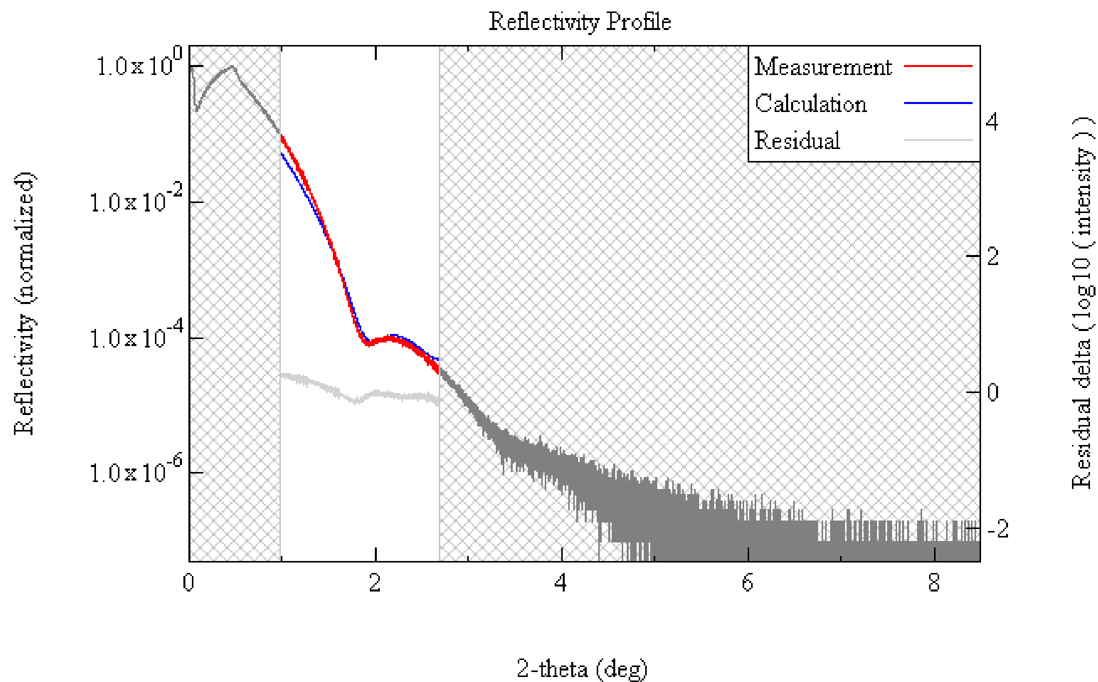

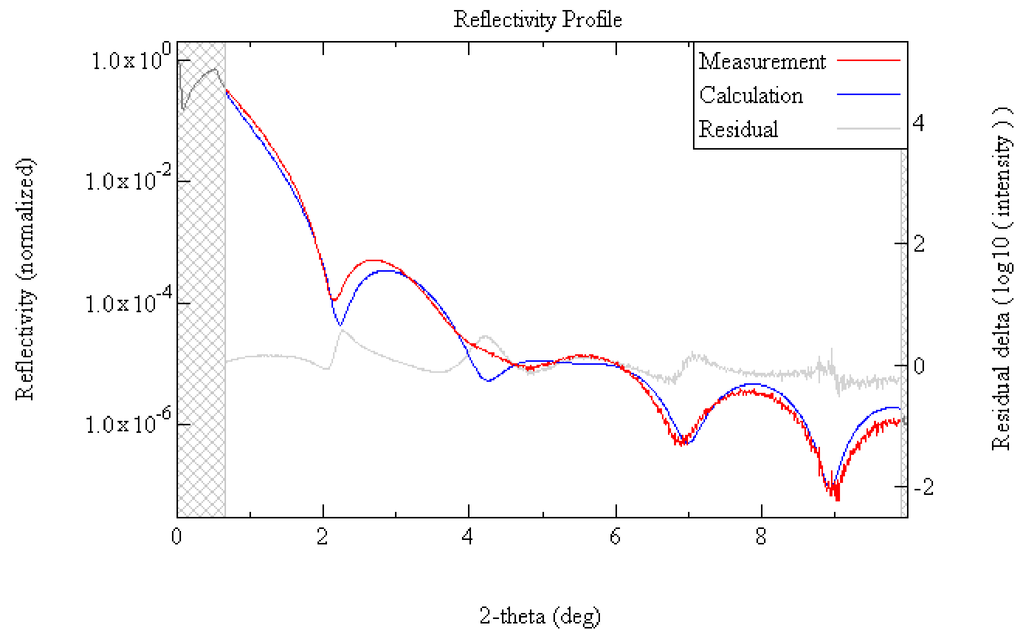

Figure 5.12: XRR measurements of NbN on SiN_x (SPE024) (a) and MgO (SPE022) (b) along with calculated XRR profiles material model. Here we can see the result of performing XRR analysis on the RTPed film on SiN_x SPE024, as well as a film on MgO that was deposited at the same time. The reflectivity profile is significantly degraded in the silicon nitride case, whereas the film on MgO shows multiple interference fringes. The best fit model for SPE024 is 4.1nm thick NbN with two nanometers of oxide on top, while the film on MgO is was best modelled as 4nm of NbN with 0.9nm of oxide. The surface roughness of the SPE024 model was fixed as 0.4nm to match the AFM data. The data fit for SPE022 was significantly worse if the oxide layer was removed from the model.

The XRR data is not the only data that suggests that our films have a cap of oxide on them. We re-measured a set of films on MgO (Rs, T_c, thickness) after up to 10 months of being stored in a nitrogen box. We observed varying degrees of increased sheet resistance, but based on the initial sheet resistance and thickness, we were able to accurately predict the new sheet resistance by simply assuming a small portion of each film had converted into a nonconductive

oxide. The remaining non-oxidized films were assumed to keep their initial resistivity, and a new sheet resistance was calculated based on an effect reduction in thickness, indicating a uniform oxide layer across different films:

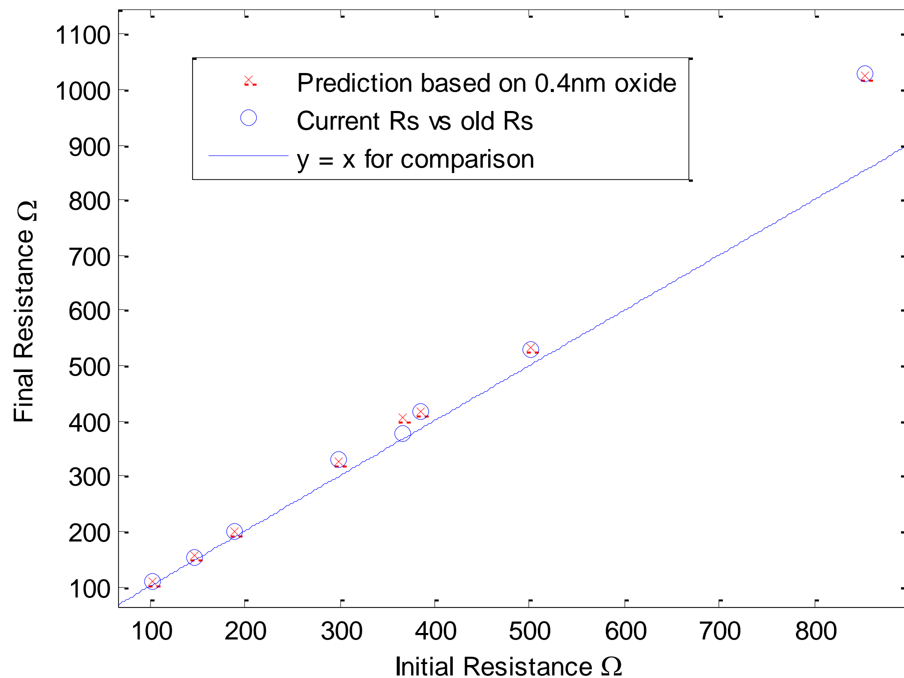

Figure 5.X Sheet resistance after up to 10 months of aging for films ranging in thickness from 2.4nm to 7.9nm. All but one of the final Rs values can be predicted by a reduction in thickness of 0.4nm, with the remaining film keeping its initial resistivity. This plus the XRR fitting give us a good idea that we have a small layer of oxide on top of our films.

Rapid Thermal Processing of Room Temperature Deposited Nb and NbN:

While the NbN that we have been able to deposit has state of the art T_c for ~4nm thick films [11], we are able to achieve this in part due to a dedicated system that can heat substrates to 800C and incorporate nitrogen for reactive sputtering. Without such a system, would we still be able to achieve these good results? We did some preliminary tests of using the RTP to nitridize

Nb films, as well as NbN films grown at room temperature. The results of nitridization is shown in Figure 5.13. Our initial experiments failed to yield good films when attempting to nitridize them using the RTP, despite the fact that this has been shown to work in thicker films. For some samples (not shown), the result of the RTP was total obliteration of the film such that there was no discernable difference between the resulting film and leaving the sheet resistance measurement system open.

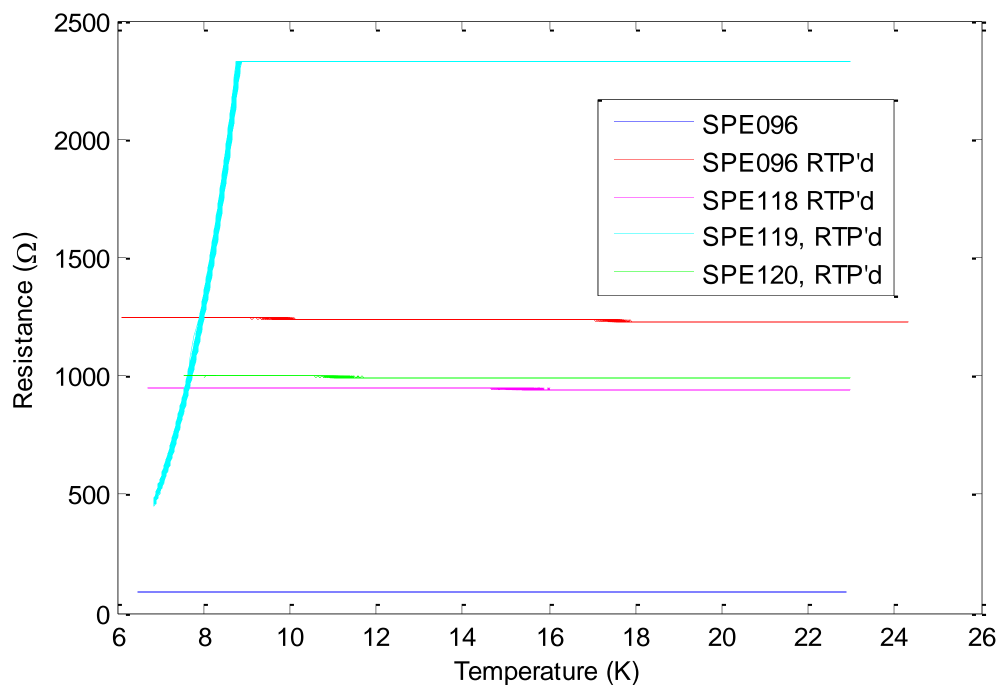

Figure 5.13: all films were deposited for 69 seconds without any nitrogen at room temperature. The resistance vs temperature for film SPE096 (blue) was typical for these Nb films before RTP. None of these Nb films uperconducted down to 6K. The RTPed films do not superconduct in the range of temperatures measured, except for SPE119 which was RTPed with a 1.5 minute hold at 1000C instead of 3 minutes in th standard process. SPE118 and 120 were RTPed to a maximum temperature of 500C for 3 and 1.5 minutes respectively. Note that the very flat curve of SPE119 above ~8.5K is an artifact of the measurement system; with a constant current being driven into a

high sheet resistance, the signal was too large after amplification and had saturated to the maximum voltage of the measurement system.

Although nitridization of Nb films in the RTP did not in general yield superconducting films, a very interesting result came from RTPing an NbN film that was deposited at room temperature and was measured before and after RTP, and is shown in Figure 5.14. The initial film did not superconduct down to less than 8K, but after applying our standard RTP recipe, this film had a T_c of ~12.9K. While it appears that starting with a higher- T_c material will result in a higher-T_c end product, the results of RTPing NbN films of a range of different T_c s are films that end up close to the neighborhood of 13K T_c. One plausible explanation to this uniformity is that RTPing is always creating $NbSi_yN_x$. If this material has a short enough coherence length then perhaps we are always creating a 3D structure out of a 2D one by scaling the coherence length (with overall crystal structure unchanged). Further work will be necessary to make any conclusions.

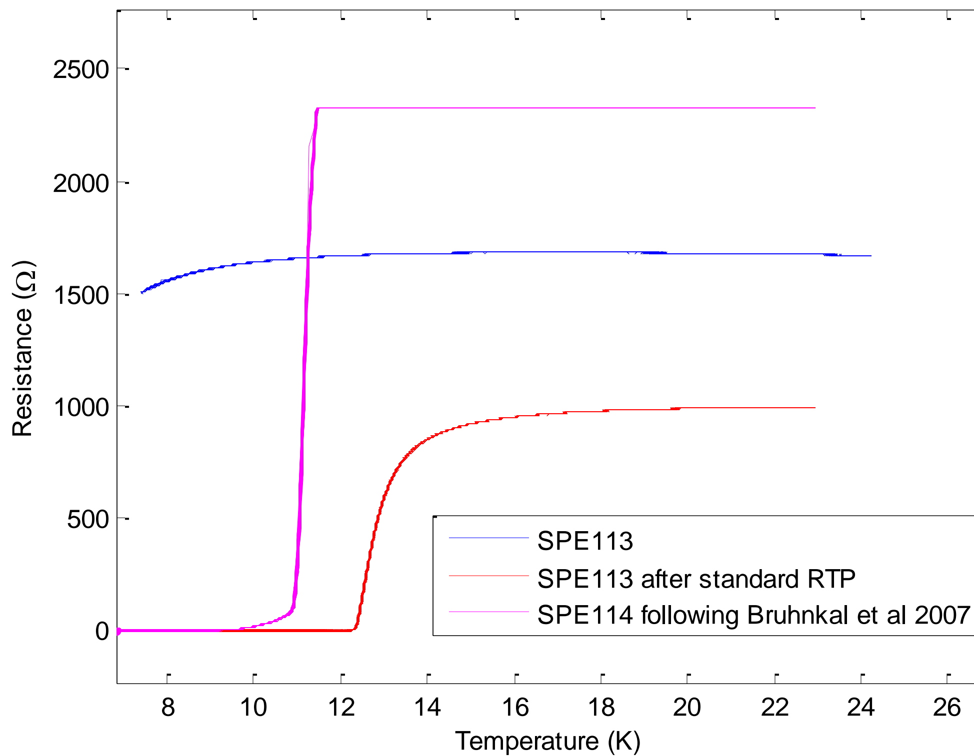

Figure 5.14: RTPing NbN grown at room temperature. SPE113 and 114 were deposited for 69 seconds similar to most of the films reported on in this work. RTPing SPE113 with our standard 1000C process ielded the surprising result of a film with 12.9K T_c. This suggests some underlying uniformity among all films that come out of the RTP as they all result in T_c s close to 13K despite starting with T_c s ranging from less than 8 to more than 11. SPE114 was RTPed in a process given in the literature but produced inferior results.

Since NbN and other Nb based superconductors are useful for a range of practical applications, annealing and RTPing of thick (~100nm) films and bulk samples has been thoroughly investigated. Most literature suggests that improved crystallinity is the cause of the increase of T_c, likely due to increased free electron density [15].

RTPing of the films has shown itself to be a successful way of increasing film T_c whatever the mechanism, but it still requires another processing step in a different tool, which is in a shared facility and outside of our control. It would be better if we could heat treat our films in the deposition chamber we already use, which is UHV and highly controlled. We attempted to anneal our films in situ after deposition, mimicking the RTP profile somewhat: heating to 800C as quickly as possible, holding for 3 minutes, and then cooling down as quickly as allowed by the system. The results are shown in Figure 5.15. In situ annealing resulted in films with lower T_c with respect to the baseline. It appears that the culprit may be the slow rate at which the substrates cool inside of the deposition system, cooling from the nominal temperature of 800C to room temperature over the course of approximately 5 hours. This is further backed by the literature, which suggests that at elevated temperatures, delta phase NbN (which has the highest T_c among polytypes) is converted into lower T_c nabla phase NbN below 1370C [16].

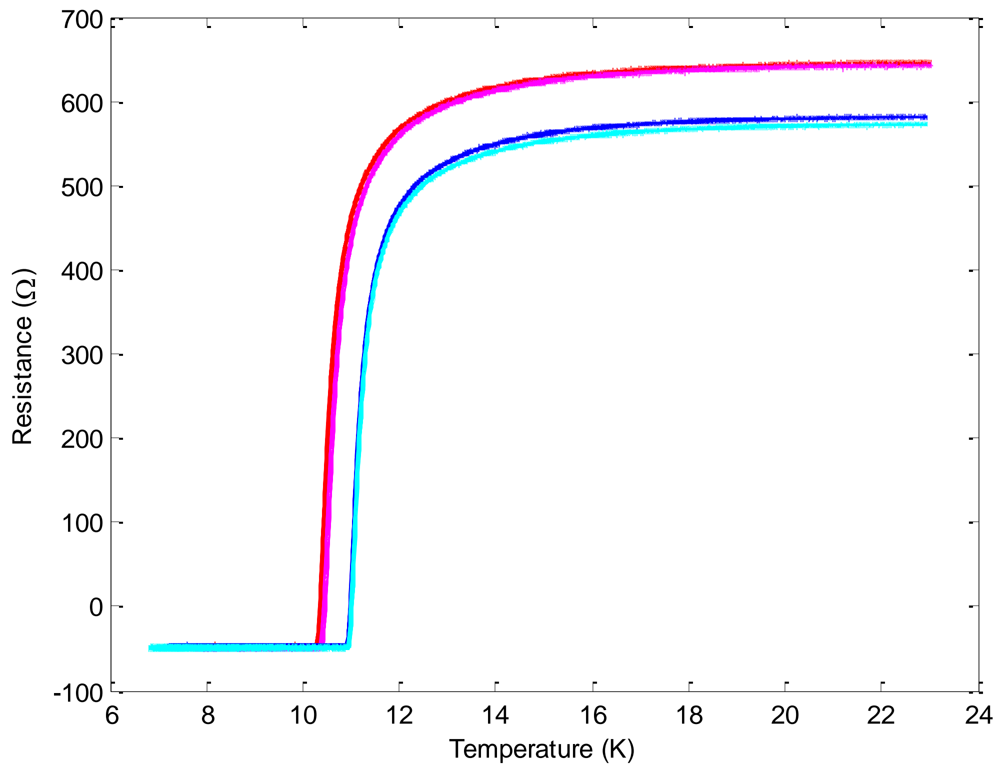

Figure 5.15: In-situ annealing of NbN films on SiN_x. Curves in red and magenta correspond to films that were grown in identical conditions to those in blue and cyan except with the addition of an RTP mimicking annealing step. These films likely have a lower T_c due to additional time spent hot enough to encourage delta phase NbN to convert to less ideal (lower T_c) phases.

The conversion of high T_c NbN to a lower Tc crystal phase after the deposition may also explain why we were previously able to increase film T_c by flooding the deposition chamber with nitrogen after deposition [17]. This flooding of the chamber likely increased the rate at which the samples cooled, suppressing growth of non-ideal crystal phases. We repeated this in a somewhat modified form—instead of venting the chamber to atmospheric pressures with nitrogen gas from a potentially dirty source (a common laboratory nitrogen line feed by high pressure liquid

nitrogen dewar), we flowed the reactive nitrogen to a pressure of 30mtorr for one hour after the deposition. The result was that we did not see a difference when adding this cooling step, though likely because this cooling was ineffective. The results are summarized in Figure 5.16.

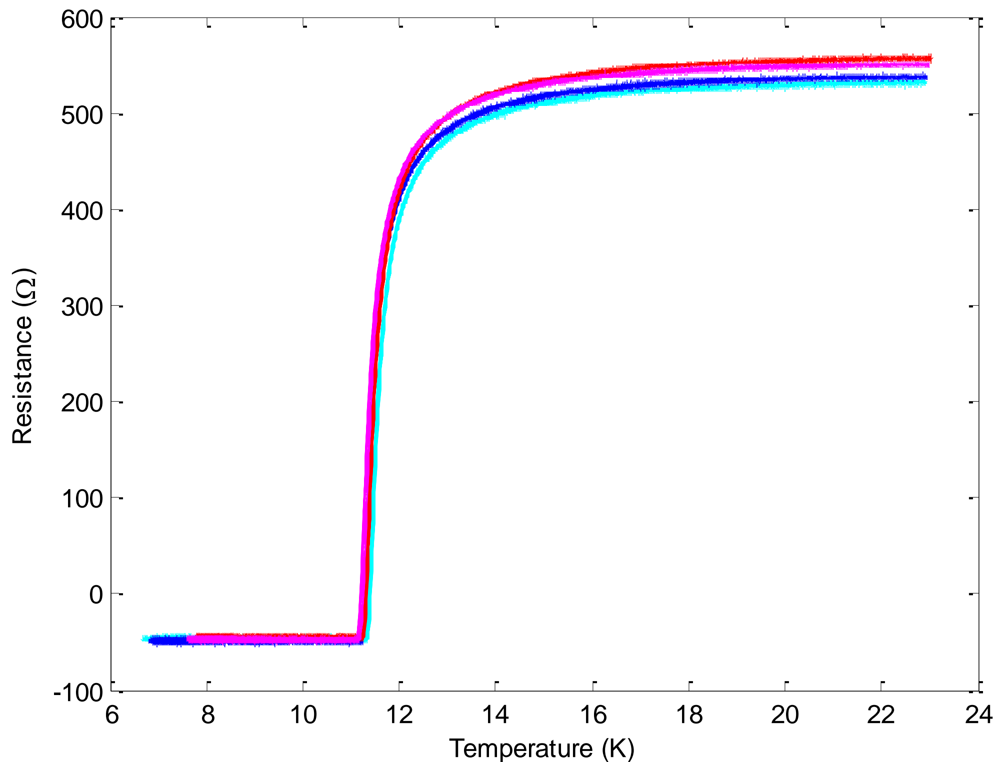

Figure 5.16: Quench cooling. Four films were deposited in two identical runs, except those films in blue and cyan had an additional processing step wherein the chamber was filled with nitrogen up to 30mtorr for one hour. This attempt at cooling had no effect on the film T_c. Previous attempts were done with extreme flow rates of Nitrogen that would require basically venting the entire chamber. We wished to avoid this.

Lastly, we attempted to make many NbN films on SiN_x at once by depositing on a 4 inch wafer (the same that are normally cut into 1cm by 1cm samples prior to their use), then dicing

this wafer and testing the resulting films. This method did not yield good films. Figure 15.17 demonstrates that films from around the wafer have a low average T_c and it is quite scattered. Because this result was so poor, no additional tests were made on whole wafers.

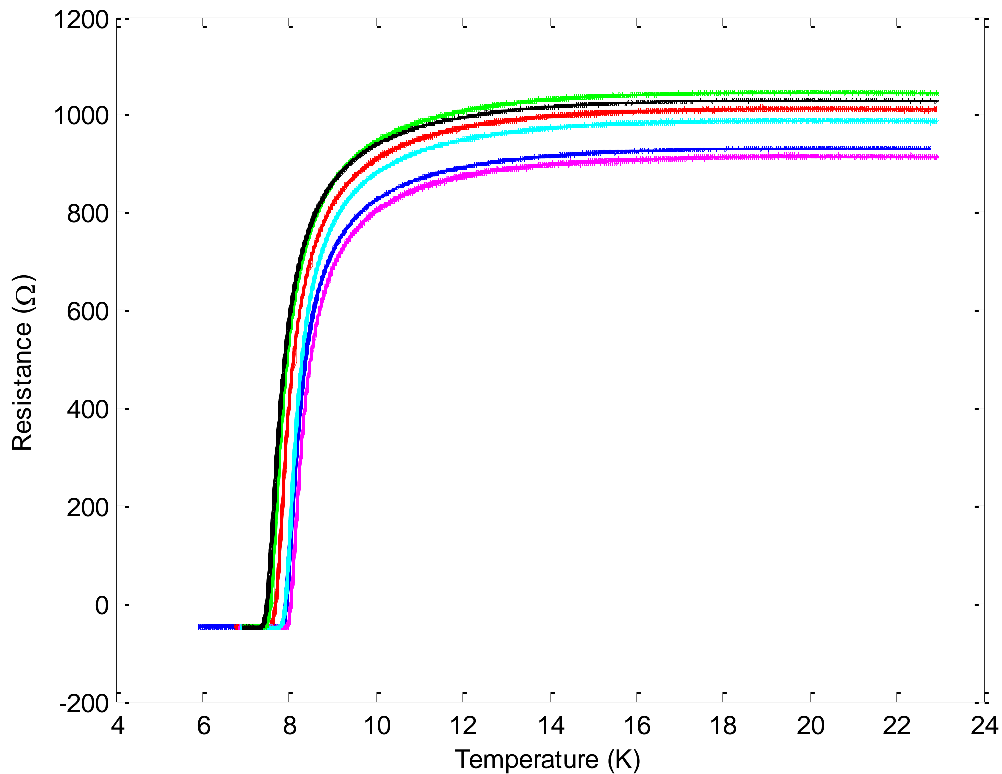

Figure 5.17: Depositing on a whole wafer. NbN was deposited for 69 seconds onto a 4 inch wafer of SiN_x on Si. The process used was identical to the baseline on Figure 5.16 and was expected to yield films with T_c close to 11K. However, we can see that that was not the case. It is unclear if this result is due to poor heating or different strain conditions.

References:

1. Kang, L., Jin, B. B., Liu, X. Y., Jia, X. Q., Chen, J., Ji, Z. M., … Wang, B. G. (2011). Suppression of superconductivity in epitaxial NbN ultrathin films. Journal of Applied Physics, 109(3), 033908. doi:10.1063/1.3518037
2. Wang, Z., Kawakami, A., Uzawa, Y., & Komiyama, B. (1996). Superconducting properties and crystal structures of single-crystal niobium nitride thin films deposited at ambient substrate temperature. Journal of Applied Physics, 79(10), 7837. doi:10.1063/1.362392
3. L. E. Toth, Transition Metal Carbides and Nitrides, Academic Press Inc (May 1971), ISBN-13: 978-0126959505
4. Operation manual AJA Orion ATC sputtering system
5. Messier, R. (1984). Revised structure zone model for thin film physical structure. Journal of Vacuum Science & Technology A: Vacuum, Surfaces, and Films, 2(2), 500. doi:10.1116/1.572604
6. Thornton, J. a. (1986). The microstructure of sputter-deposited coatings. Journal of Vacuum Science & Technology A: Vacuum, Surfaces, and Films, 4(6), 3059. doi:10.1116/1.573628
7. Windischmann, H. (1992). Intrinsic stress in sputter-deposited thin films. Critical Reviews in Solid State and Materials Sciences, 17(6), 547–596. doi:10.1080/10408439208244586
8. Hoffman, D. W. (1994). Perspective on stresses in magnetron-sputtered thin films. Journal of Vacuum Science & Technology A: Vacuum, Surfaces, and Films, 12(4), 953. doi:10.1116/1.579073

9. Tanabe, K., Asano, H., Katoh, Y., & Michikami, O. (1988). Ellipsometric and optical reflectivity studies of reactively sputtered NbN thin films. Journal of Applied Physics, 63(5), 1733. doi:10.1063/1.339910
10. K. Sunter, PhD Thesis, MIT, 2014
11. Gao, J. R., Hajenius, M., Tichelaar, F. D., Klapwijk, T. M., Voronov, B., Grishin, E., … Mehregany, M. (2007). Monocrystalline NbN nanofilms on a 3C-SiC/Si substrate. Applied Physics Letters, 91(6), 062504. doi:10.1063/1.2766963
12. Guziewicz, M., Slysz, W., Borysiewicz, M., Kruszka, R., Sidor, Z., Juchniewicz, M., … Sobolewski, R. (2011). Technology of Ultrathin NbN and NbTiN Films for Superconducting Photodetectors. ACTA PHYSICA POLONICA A, 120(6), 76–79.Slysz, 2010
13. Słysz, W., Guziewicz, M., Borysiewicz, M., Domagała, J. Z., & Pasternak, I. (2011). Ultrathin NbN Films for Superconducting Single-Photon Detectors. ACTA PHYSICA POLONICA A, 120(1), 200–203.
14. Chockalingam, S., Chand, M., Jesudasan, J., Tripathi, V., & Raychaudhuri, P. (2008). Superconducting properties and Hall effect of epitaxial NbN thin films. Physical Review B, 77(21), 214503. doi:10.1103/PhysRevB.77.214503
15. Linde et al, "Effect of Nitrogen to Niobium Atomic Ratio on Superconducting Transition Temperature of δNbNx Powders," ISSN 10613862, International Journal of SelfPropagating HighTemperature Synthesis, 2010, Vol. 19, No. 1, pp. 9–16
16. L. Schonenberg, Characterization of the Superconducting Transition in Disordered NbN S.B. Thesis, Delft University, 2012

Chapter 6

Future Work:

A number of open questions remain after the completion of this work, they include: (1) what is the origin of the excess resistivity in NbN on amorphous substrates relative to its bulk form, (2) how can rapid thermal processing be used to understand the relationship between resistivity and Tc, (3) can we modify Berg's model to adequately predict IV curves observed during the reactive sputter deposition of NbN, (4) what is the interplay between crystallinity, chemistry and deposition parameters for NbN and how do we quantify their effects on film Tc, (5) can we establish a nanoscale structure zone model that is generally useful.

Resistivity in thin films of a material is often higher than the bulk resistivity and a variety of models have been put forth to capture the size effects that are important. Chronologically, the first such model included the effect of electrons scattering off of the surfaces of the film (Fuchs and Sondheimer model), later scattering from grain boundaries was added (Mayadas Model), and later still the shape of the films surface was included (Nambu Model) [1]. Since the mean free path in NbN is only 4 Angstroms, making the FS model unlikely, and since the resistance of thin films tends to rise in response to lowering the temperature, the conclusion is often that weak coupling between grains is the culprit for increased resistivity at low thickness. This has not be adequately explored in few nanometer thick films, nor has surface morphology's contribution to resistivity. Additionally, while it appears that bulk resistivity is reached in lattice matched films

on MgO of sufficient thickness, the resistivity of our films on SiN and SiO2 is a few times higher at the same thickness. While it's easy to say that this is the result of highly disorder dead layers at the interface, it is less easy to quantify the effect of these dead layers on the Tc of the film. Thus studies of disorder's effects on NbN Tc do not include grain boundary scattering and typically assume a free electron model when attempting to derive the useful parameters of the system [2].

Recently, annealing of amorphous NbSi films was used to explore the separate effects of thickness and sheet resistance on T_c [3]. Annealing was done for short periods of time and at low enough temperatures that the amorphous NbSi did not crystalize, as shown by x-ray diffraction and surface morphology. By varying the anneal temperature, a variety of sheet resistances could develop from the same initial film thickness and Tc and it was argued to be a tuning parameter for disorder in the film (along with the chemical composition). At a given thickness, sheet resistance was adequate to fully explain different Tc, but it was not for changing thicknesses. This is interesting to compare with our RTP'd NbN films. For both, composition has been argued as a tuning parameter for disorder. For NbSi, annealing at higher temperature increases R_s and reduces T_c. On the other hand, RTP of polycrystalline NbN leads to an increase in Tc with the possibility of increased or decreased R_s. The mechanisms responsible may be completely different, but nonetheless an avenue for changing resistivity and Tc exists for both and likely others, and may help disentangle their relationship. Another major, and perhaps the most important difference in the case of NbN, was that RTP'd films that started off with a variety of compositions ended up with a Tc of 13K, rather than a spectrum of values depending on initial conditions. This increase of the film T_c to 13K after RTP is corroborated by existing studies of RTP on NbN.

It has been observed frequently in sputter deposited NbN films that the maximum Tc is a function of nitrogen flow and total pressure, with the maximum Tc rising as the system pressure is dropped, and a clear maximum in Tc developing as nitrogen flow is varied. While we can likely call these deposition parameters proxies for the film stoichiometry and the film crystallinity, an adequate description of the various Tc vs Nitrogen flow and system pressure is still absent. It may be possible, as in the case of neutron damaged NbN films, to quantify this relationship in the form of valence electrons per atom as determining the film Tc. There is likely a more general and useful theory that can be used to explain this behavior and help illuminate the role of disorder on Tc in general.

A simple but useful extension of Berg's model is the inclusion of a varying secondary electron coefficient to model the deposition voltage at fixed current and varying reactive gas flow rate. A use of a model like this is to predict the IV curves seen during NbN deposition at different Nitrogen flow rates and power levels, thus characterizing the plasma impedance for a given deposition system. This modeling and the relevant parameters that fall out of it could help make process transfer among system easier.

Lastly, while incredibly useful in a qualitative way, the structure zone models are generally formulated and concerned with films that are thicker than those studied here. An extensive study of NbN films at a few nanometers thickness with TEM could allow the development of a useful nanoscopic structure zone model of general utility.

References:

1. Liu, H., Zhao, Y., Ramanath, G., Murarka, S. P., & Wang, G. C. (2001). Thickness dependent electrical resistivity of ultrathin (<40 nm) Cu films. Thin Solid Films, 384, 151–156.
2. Chockalingam, S., Chand, M., Jesudasan, J., Tripathi, V., & Raychaudhuri, P. (2008). Superconducting properties and Hall effect of epitaxial NbN thin films. Physical Review B, 77(21), 214503. doi:10.1103/PhysRevB.77.214503
3. Crauste, O., Gentils, a., Couëdo, F., Dolgorouky, Y., Bergé, L., Collin, S., … Dumoulin, L. (2013). Effect of annealing on the superconducting properties of a-Nb_{x}Si_{1-x} thin films. Physical Review B, 87(14), 144514. doi:10.1103/PhysRevB.87.144514